J. Fluid Mech. (2011), *vol.* 681, *pp.* 48–79. © Cambridge University Press 2011
doi:10.1017/jfm.2011.170

Direct and large-eddy simulations of internal tide generation at a near-critical slope

BISHAKHDATTA GAYEN AND SUTANU SARKAR†

Mechanical and Aerospace Engineering, University of California, San Diego, La Jolla, CA 92093, USA

(Received 18 October 2010; revised 5 February 2011; accepted 1 April 2011;
first published online 25 May 2011)

A numerical study is performed to investigate nonlinear processes during internal wave generation by the oscillation of a background barotropic tide over a sloping bottom. The focus is on the near-critical case where the slope angle is equal to the natural internal wave propagation angle and, consequently, there is a resonant wave response that leads to an intense boundary flow. The resonant wave undergoes both convective and shear instabilities that lead to turbulence with a broad range of scales over the entire slope. A thermal bore is found during upslope flow. Spectra of the baroclinic velocity, both inside the boundary layer and in the external region with free wave propagation, exhibit discrete peaks at the fundamental tidal frequency, higher harmonics of the fundamental, subharmonics and inter-harmonics in addition to a significant continuous part. The internal wave flux and its distribution between the fundamental and harmonics is obtained. Turbulence statistics in the boundary layer including turbulent kinetic energy and dissipation rate are quantified. The slope length is varied with the smaller lengths examined by direct numerical simulation (DNS) and the larger with large-eddy simulation (LES). The peak value of the near-bottom velocity increases with the length of the critical region of the topography. The scaling law that is observed to link the near-bottom peak velocity to slope length is explained by an analytical boundary-layer solution that incorporates an empirically obtained turbulent viscosity. The slope length is also found to have a strong impact on quantities such as the wave energy flux, wave energy spectra, turbulent kinetic energy, turbulent production and turbulent dissipation.

Key words: internal waves, stratified turbulence

1. Introduction

Tides in the ocean interact with bottom topography to result in energetic internal gravity waves, the so-called internal tides. It is thought that internal tides play an important role in deep ocean mixing (Polzin *et al.* 1997; Munk & Wunsch 1998; Ledwell *et al.* 2000; Wunsch & Ferrari 2004). The conversion to internal tides is enhanced by sea-mounts (Lueck & Mudge 1997; Kunze & Toole 1997), submarine ridges (Rudnick *et al.* 2003; Klymak *et al.* 2006), submarine canyons (Polzin *et al.* 1996; Carter & Gregg 2002), continental slope (Cacchione, Pratson & Ogston 2002; Moum *et al.* 2002; Nash *et al.* 2004; Nash *et al.* 2007) and deep rough topography (Polzin *et al.* 1997; St Laurent, Toole & Schmitt 2001). As part of the baroclinic response to an oscillating flow over sloping topography shown schematically in

† Email address for correspondence: ssarkar@ucsd.edu

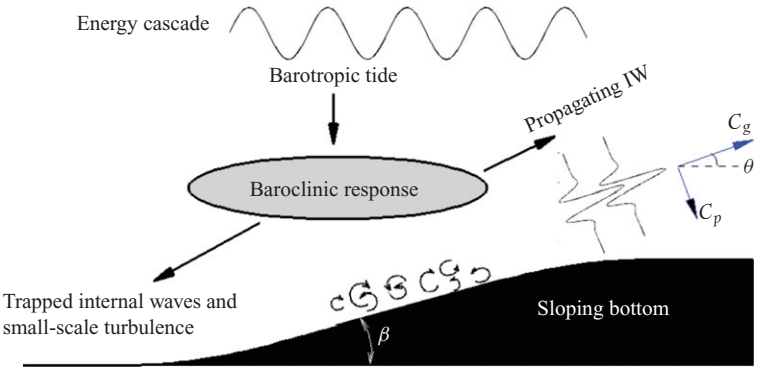

FIGURE 1. (Colour online available at journals.cambridge.org/flm) Schematic diagram of the near-slope energy cascade during generation of internal waves at sloping topography of angle β. Here, C_p denotes phase velocity and C_g denotes group velocity.

figure 1, energy propagates out as internal waves while some energy is locally confined as trapped internal wave motion and a bottom boundary layer. The locally confined energy may cascade to small-scale turbulence owing to nonlinear effects that can be especially large when the slope angle is near the critical value. The propagating internal waves can also break down to turbulence at sites remote from the generation region through a variety of mechanisms including reflection at a topographic slope with critical angle. The case of critical and near-critical reflection of waves incident on a slope has been studied in the laboratory, by analysis and direct numerical simulation (DNS) of the three-dimensional Navier–Stokes equations. Laboratory studies (Ivey & Nokes 1989; Thorpe 1992) and DNS studies (Slinn & Riley 1998; Venayagamoorthy & Fringer 2007) of internal wave reflection find that wave/slope interactions lead to a complex turbulent flow. Here, we investigate a different problem, that of internal wave generation rather than internal wave reflection, using both DNS and large eddy simulation (LES).

Generation of internal waves at sloping topography is governed by the following physical parameters as discussed by Garrett & Kunze (2007): frequency of tidal oscillation Ω, the buoyancy frequency N_∞, the Coriolis frequency f, the topographic height h and horizontal length l, the depth of the ocean, H, and the amplitude of the deep-water barotropic tidal velocity U_0. Two important non-dimensional parameters are: (i) the criticality parameter, $\epsilon = \tan(\beta)/\tan\theta$, which is the ratio of the topographic slope $\tan(\beta)$ to the slope of internal wave characteristic $\tan\theta = \sqrt{(\Omega^2 - f^2)/(N_\infty^2 - \Omega^2)}$; (ii) the excursion number, $Ex = U_0/\Omega l$. The response at harmonics of the tidal frequency increases when Ex increases. Values of Ex are typically $\ll 1$ in the ocean except for some coastal regions where the topography is steep and the barotropic tides are strong. Topography is said to be subcritical, critical or supercritical if $\epsilon <, =$ or > 1. Nonlinear effects in the wave response become increasingly important when ϵ is finite and cannot be assumed to be much smaller than unity. The case with $\epsilon = 1$ is a resonant situation where viscous dissipation, possibly in conjunction with turbulence, regularizes the near-boundary response. The present study is restricted to near-critical slope angles with $\epsilon \simeq 1$ and low excursion number $Ex \ll 1$. Under such circumstances, the internal wave energy that leaves the topography is concentrated into a tidal beam as shown in figure 2, and the near-bottom velocity is strongly intensified with respect to the barotropic tidal amplitude.

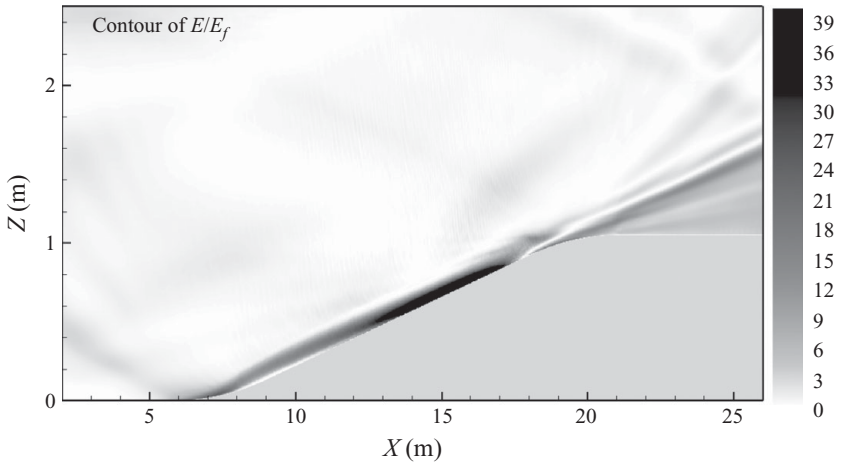

FIGURE 2. Contours of the kinetic energy, E, in a case simulated to illustrate the formation of a beam of internal waves. Normalization is with respect to the barotropic kinetic energy, E_f.

The linear theory of internal tides is well developed. A popular theoretical approach is based on the weak topography approximation (WTA), i.e. height changes in topography are small compared to the depth of the ocean and the topographic slope is small relative to the slope of internal wave phase lines. Bell (1975*a*, *b*) decomposed the topography into Fourier modes, introduced WTA, and computed the energy conversion rate in a uniformly stratified, infinitely deep ocean by linear superposition. St Laurent & Garrett (2002) used the analysis of Bell to deduce that the conversion from barotropic to internal tide is significant at the Mid-Atlantic Ridge and, under the assumption of linear theory, found that most of the internal wave energy resides in low modes which propagate away without dissipating locally. Llewellyn Smith & Young (2002), Balmforth, Ierley & Young (2002) and Khatiwala (2003) further developed WTA to estimate the tidal conversion in other types of subcritical topography while allowing for finite depth and non-uniform stratification. Balmforth *et al.* (2002) performed a perturbative expansion in the parameter ϵ to estimate the influence of increasing slope steepness. Their solution showed a singularity in the solution when $\epsilon \geqslant 1$. All the aforementioned theories are accurate for small-amplitude subcritical topography. In a different approach, Baines (1974, 1982) developed an analytical model based on ray theory and wave characteristics. This model can deal with arbitrary topography including steep, supercritical topography as long as the regions with $\epsilon = 1$ can be approximated as isolated critical points. Llewellyn Smith & Young (2003) revisited the problem of steep topography using a Green's function approach (Robinson 1969) to deal with the singularity at $\epsilon = 1$. Other studies (St Laurent *et al.* 2003; Pétrélis, Llewellyn Smith & Young 2006; Balmforth & Peacock 2009) estimated the conversion rate for arbitrary-shaped topography; among them Pétrélis *et al.* (2006) calculated a finite value of conversion rate at near-critical topography although velocity and density were found to be singular. Griffiths & Grimshaw (2007) employed a modal approach where the flow field is expanded in terms of basis functions newly derived by the authors. The number of modes required for a converged solution was found to be small, less than 10, for $\epsilon < 1$. However, the solution for $\epsilon \geqslant 1$ contains singular beams so that finer structure is revealed with increasing number of modes.

Wave generation in the form of a localized beam has been studied in laboratory experiments that consider model continental slopes (Gostiaux & Dauxois 2007; Zhang, King & Swinney 2008; Lim, Ivey & Jones 2010) and other underwater model topography (Echeverri *et al.* 2009). Zhang *et al.* (2008) focused on the case with critical slope and found that the resonant wave/slope interaction led to a laminar oscillating boundary layer with intensified bottom velocity, an order of magnitude larger than the imposed oscillatory forcing. All the laboratory studies of internal wave generation have been conducted at low Reynolds number ($Re \sim O(1)$) with the notable exception of Lim *et al.* (2010), who find beam formation, boundary-layer turbulence and upslope propagation of bores depending on the value of the Reynolds number.

Nonlinear ocean models have proved effective in studying internal tides in a realistic oceanic environment. Holloway & Merrifield (1999) used the nonlinear hydrostatic Princeton Ocean Model (POM) to demonstrate that the conversion into internal wave energy is stronger for flow across elongated features such as ridges rather than symmetric features such as islands and seamounts. The POM calculations of Merrifield, Holloway & Johnston (2001) identified key generation sites at the Hawaiian Ridge and showed multiple dynamical modes in the near field. Legg (2004) used the Massachusetts Institute of Technology (MIT) model to perform three-dimensional simulations of generation from a continental slope in a regime with $Ex \ll 1$ but with steep topography including critical and supercritical regions. Along-slope corrugations in the slope were identified as important for realizing high-mode internal waves with potential for local mixing. Legg & Klymak (2008) performed two-dimensional calculations of flow over a tall steep ridge and showed that, at the top of the ridge, the intensified barotropic flow in conjunction with a large slope angle leads to overturning events associated with transient internal hydraulic jumps. Korobov & Lamb (2008) have examined the frequency content of the propagating internal wave field to show the generation of subharmonics, higher harmonics and interharmonics during tide/topography interaction.

The turbulent boundary layer on a *non-sloping* flat bottom under an oscillating current has been examined in the unstratified case by simulations that resolve turbulence. DNS studies (Spalart & Bladwin 1987; Akhavan, Kamm & Shapiro 1991; Vittori & Verzicco 1998; Costamagna, Vittori & Blondeaux 2003; Sakamoto & Akitomo 2008) have paid attention primarily to the disturbed laminar and intermittently turbulent flow regimes that occur at moderate values of the Reynolds number. The LES approach has allowed studies in the fully turbulent regime. The simulations of Salon, Armenio & Crise (2007) performed with a dynamic mixed model agreed well with the experimental results of Jensen, Sumer & Fredsøe (1989) and provided new insights into the phase dependence of inner- and outer-layer turbulence. Radhakrishnan & Piomelli (2008) have performed LES with various subgrid models and near-wall treatments to further extend the Reynolds number of the simulations. Turbulence-resolving simulations of oceanic bottom boundary layers in a stratified fluid are scarce. Taylor & Sarkar (2008*a*) examined the thermal field in a stratified boundary layer using both DNS and LES, and Taylor & Sarkar (2008*b*) showed that stratification has a significant effect on boundary-layer thickness and structure. Broadband bottom turbulence was found to lead to internal waves which tended to cluster around 45° during propagation as discussed by Taylor & Sarkar (2007). An oscillating boundary layer in a stratified fluid was examined through LES by Gayen, Sarkar & Taylor (2010), who found that stratification increases the asymmetry in turbulence between accelerating and decelerating phases and also increases the

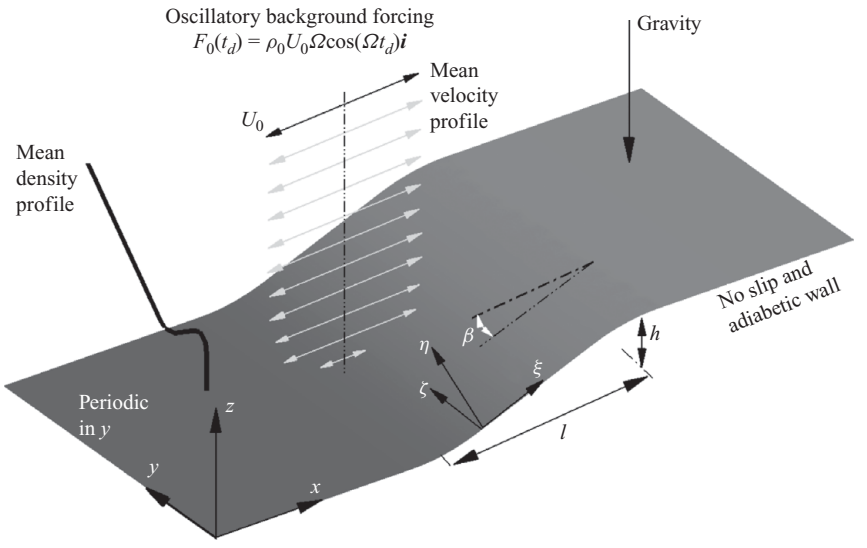

FIGURE 3. Schematic diagram of the problem. Stratified fluid flows over sloping topography as a response to oscillatory forcing, $F_0(t_d)$, in the streamwise direction.

height-dependent lag in the phase of maximum turbulent kinetic energy with respect to the peak free-stream velocity. Li *et al.* (2010) employed LES to study an estuarine tidal boundary layer where the horizontal density gradient associated with salinity is found to introduce a strong ebb–flood asymmetry in the turbulence.

Since all the theoretical investigations of internal tide generation are based on linear analysis, they cannot study the evolution of flow instabilities into turbulence. Previous numerical models of internal tide generation have proved useful for studying some nonlinear aspects of the generation problem but the relatively coarse resolution and high values of viscosity in these simulations preclude resolution of turbulence dynamics. Recently, Gayen & Sarkar (2010) performed a three-dimensional DNS of generation by a laboratory-scale slope in the regime of $Ex \ll 1$ and $\epsilon \simeq 1$ that shows transition to turbulence along the entire slope. The transition is found to be initiated by a convective instability which is closely followed by shear instability. The present simulations extend the work of Gayen & Sarkar (2010) by examining internal wave energetics as well as the energetics of turbulence in the bottom boundary layer. In addition, the effect of increasing slope length, l, is quantified by employing an LES approach to access higher values of l. The present work also extends previous DNS/LES of bottom turbulence from the case of tidal flow over a non-sloping bottom to the situation with a sloping bottom where the baroclinic wave velocity dominates the barotropic tidal velocity.

2. Formulation of the problem

The near-bottom flow resulting from a current oscillating on an inclined surface is illustrated in figure 3. The bottom is adiabatic while there is a background thermal stratification with constant buoyancy frequency, N_∞. The flow is forced by an imposed pressure gradient,

$$F_0(t_d) = \rho_0 U_0 \Omega \cos(\Omega t_d), \tag{2.1}$$

in the horizontal direction that results in a background barotropic current, $U(x)\sin(\phi)$, where ϕ is the tidal phase. In the figure, coordinates x, y and z denote the horizontal, spanwise and vertical directions and u, v and w are the corresponding velocity components, while ξ, ζ and η are curvilinear coordinates employed in the simulation.

2.1. *Governing equations*

The Navier–Stokes equations, under the Boussinesq approximation, which are numerically solved here are written as follows with dimensional form denoted by subscript d:

$$\nabla\cdot\boldsymbol{u}_d = 0, \tag{2.2a}$$

$$\frac{\mathrm{D}\boldsymbol{u}_d}{\mathrm{D}t_d} = -\frac{1}{\rho_0}\nabla p_d^* + \frac{F_0(t_d)}{\rho_0}\boldsymbol{i} + \nu\nabla^2\boldsymbol{u}_d - \frac{g\rho_d^*}{\rho_0}\boldsymbol{k} - \nabla\cdot\boldsymbol{\tau}_d, \tag{2.2b}$$

$$\frac{\mathrm{D}\rho_d}{\mathrm{D}t_d} = \kappa\nabla^2\rho_d - \nabla\cdot\boldsymbol{\lambda}_d. \tag{2.2c}$$

Rotation is not included, for simplicity. Here, p_d^* denotes deviation from the background hydrostatic pressure and ρ_d^* denotes the deviation from the linear background state, $\rho_d^b(z_d)$. In the LES mode, $\boldsymbol{u}_d$ and ρ_d are to be interpreted in the equations as filtered quantities, i.e. we drop the overbar conventionally used to denote filtering. Here $\boldsymbol{\tau}_d$ and $\boldsymbol{\lambda}_d$ which are the subgrid-scale (SGS) stress tensor and density flux vector, respectively, require models for closure in LES. In DNS cases, $\boldsymbol{\tau}_d$ and $\boldsymbol{\lambda}_d$ are zero. An evolution equation for ρ_d^*, the deviation from the linear background state $\rho_d^b(z_d)$, is written as

$$\frac{\mathrm{D}\rho_d^*}{\mathrm{D}t_d} = \kappa\nabla^2\rho_d^* - w_d\frac{\mathrm{d}\rho_d^b}{\mathrm{d}z_d} - \nabla\cdot\boldsymbol{\lambda}_d. \tag{2.3}$$

The dimensional quantities in the problem are the free-stream velocity amplitude U_0, tidal frequency Ω, background density gradient $\mathrm{d}\rho_d^b/\mathrm{d}z_d|_\infty$, and the fluid properties: molecular viscosity, ν, thermal diffusivity, κ, and density, ρ.

We numerically solve the dimensional equations (2.2*a*), (2.2*b*) and (2.3). Nevertheless, it is useful to examine the non-dimensional equation. The variables in the problem are non-dimensionalized as follows:

$$\left.\begin{aligned} t = t_d\Omega, \qquad \boldsymbol{x} = (x, y, z) = \frac{(x_d, y_d, z_d)}{U_0/\Omega}, \qquad p^* = \frac{p_d^*}{\rho_o U_o^2}, \\ \boldsymbol{u} = (u, v, w) = \frac{(u_d, v_d, w_d)}{U_0}, \qquad \rho^* = \frac{\rho_d^*}{-\dfrac{U_0}{\Omega}\dfrac{d\rho_d^b}{dz_d}\bigg|_\infty}. \end{aligned}\right\} \tag{2.4}$$

The resulting non-dimensional form of the governing equations is

$$\nabla\cdot\boldsymbol{u} = 0, \tag{2.5a}$$

$$\frac{\mathrm{D}\boldsymbol{u}}{\mathrm{D}t} = -\nabla p^* + \cos(t)\boldsymbol{i} + \frac{1}{Re}\nabla^2\boldsymbol{u} - B\rho^*\boldsymbol{k} - \nabla\cdot\boldsymbol{\tau}, \tag{2.5b}$$

$$\frac{\mathrm{D}\rho^*}{\mathrm{D}t} = \frac{1}{Re\ Pr}\nabla^2\rho^* + w - \nabla\cdot\boldsymbol{\lambda}. \tag{2.5c}$$

The governing equations have three non-dimensional parameters: Reynolds number Re, Buoyancy parameter B, and Prandtl number Pr, where

$$Re \equiv \frac{aU_0}{\nu} = \frac{U_0^2}{\Omega\nu}, \quad B \equiv -g\frac{\mathrm{d}\rho_d^b}{\mathrm{d}z_d}\bigg|_\infty \frac{1}{\rho_0\Omega^2} = \frac{N_\infty^2}{\Omega^2}, \quad Pr \equiv \frac{\nu}{\kappa}. \tag{2.6}$$

Here, $a = U_0/\Omega$ is the tidal excursion length and N_∞ is the background value of buoyancy frequency assumed constant. The following Reynolds number,

$$Re_s = \frac{U_0\delta_s}{\nu} = \sqrt{2Re}, \tag{2.7}$$

based on the Stokes boundary-layer thickness, $\delta_s = \sqrt{2\nu/\Omega}$, is a commonly used alternative to Re. We employ Re_s rather than Re_δ to denote the Stokes–Reynolds number since, in geophysical boundary layers, the latter expression is often used for definitions involving the friction velocity. The slope geometry is given by the slope angle, β, and the slope length in the x-direction, l. The angle of the internal wave phase lines with the horizontal is given in a non-rotating environment by $\theta = \tan^{-1}\sqrt{\Omega^2/(N_\infty^2 - \Omega^2)}$. Thus, in addition to those listed in (2.6), there are three other non-dimensional parameters: the excursion parameter $Ex = U_0/(l\Omega)$, the slope angle β and the slope criticality parameter, $\epsilon = \tan(\beta)/\tan(\theta)$.

The Navier–Stokes equations are written in the following coordinates:

$$\xi = \xi(x, z), \quad \eta = \eta(x, z), \quad \zeta = \zeta(y), \tag{2.8}$$

where, at the slope, ξ points parallel to and across the slope while η is normal to the slope as shown in figure 3. Now (2.5) is transformed as described by Fletcher (1991) to the form of a strong conservation law as

$$\frac{\partial U_j^c}{\partial \xi_j} = 0, \tag{2.9a}$$

$$\frac{\partial(J^{-1}u_i)}{\partial t} + \frac{\partial F_{ij}}{\partial \xi_j} = J^{-1}\cos(t)\delta_{1i} - J^{-1}B\rho^*\delta_{3i}, \tag{2.9b}$$

$$\frac{\partial(J^{-1}\rho^*)}{\partial t} + \frac{\partial H_j}{\partial \xi_j} = J^{-1}w, \tag{2.9c}$$

where the fluxes are

$$F_{ij} = U_j^c u_i + J^{-1}\frac{\partial \xi_j}{\partial x_i}p^* - \frac{1}{Re}G^{jm}\frac{\partial u_i}{\partial \xi_m} + J^{-1}\frac{\partial \xi_j}{\partial x_m}\tau_{im}, \tag{2.10}$$

$$H_j = U_j^c\rho^* - \frac{1}{Re\ Pr}G^{jm}\frac{\partial \rho*}{\partial \xi_m} + J^{-1}\frac{\partial \xi_j}{\partial x_m}\lambda_m. \tag{2.11}$$

Here J^{-1}, the inverse of the determinant of the Jacobian, is the volume of the cell in physical space, U_j^c is the volume flux (contravariant velocity multiplied by J^{-1}) normal to the surface of constant ξ_j and G^{jm} is called the 'mesh skewness tensor'. These quantities are

$$U_j^c = J^{-1}\frac{\partial \xi_j}{\partial x_i}u_i, \tag{2.12}$$

$$J = \det\left(\frac{\partial \xi_j}{\partial x_i}\right), \tag{2.13}$$

$$G^{jm} = J^{-1}\frac{\partial \xi_j}{\partial x_n}\frac{\partial \xi_m}{\partial x_n}. \tag{2.14}$$

Here, repeated indices represent implied summation.

2.2. Numerical method

Boundary conforming grid generation based on transfinite interpolation (TFI) has been used. In this method, the domain boundary points are specified through four sets of parametric equations,

$$\boldsymbol{x}_b(\xi),\ \boldsymbol{x}_t(\xi), \quad 0 \leqslant \xi \leqslant 1, \tag{2.15a}$$

$$\boldsymbol{x}_l(\eta),\ \boldsymbol{x}_r(\eta), \quad 0 \leqslant \eta \leqslant 1. \tag{2.15b}$$

Here subscripts b, t, l and r of $\boldsymbol{x} = [x, z]$ denote bottom, top, left and right boundaries, respectively. The interior grid is created from knowledge of the boundary points by using the TFI technique as follows:

$$\begin{aligned}\boldsymbol{x}(\xi,\eta) = {} & (1-\eta)\boldsymbol{x}_b(\xi) + \eta\boldsymbol{x}_t(\xi) + (1-\xi)\boldsymbol{x}_l(\eta) + \xi\boldsymbol{x}_r(\eta) \\ & -\xi\eta\boldsymbol{x}_t(1) - \xi(1-\eta)\boldsymbol{x}_b(1) - \eta(1-\xi)\boldsymbol{x}_t(0) \\ & -(1-\xi)(1-\eta)\boldsymbol{x}_b(0).\end{aligned} \tag{2.16}$$

After grid generation by the TFI method, the grid is non-orthogonal. However, at the bottom boundary conforming to the topography, an orthogonal grid is convenient to impose accurately the condition of zero-normal heat flux. So points on the two rows of points just above the bottom boundary are shifted sideways to make the η coordinate lines perpendicular to the ξ coordinate lines at the boundary. This simple process ensures grid orthogonality at the bottom boundary. The physical domain boundaries at top, left and right are such that grids are orthogonal at those boundaries.

The simulations use a mixed spectral/finite-difference algorithm. Derivatives in the spanwise direction are treated with a pseudo-spectral method and derivatives in the vertical and streamwise directions are computed with second-order finite differences. A low-storage third-order Runge–Kutta–Wray method is used for time stepping, except for the viscous terms which are treated implicitly with the alternating direction implicit (ADI) method. The eddy viscosity and diffusivity coefficients, ν_T and κ_T defined later by (2.21) and (2.22), are computed using current values of velocity and temperature. The subgrid eddy fluxes involving ν_T and κ_T are included in the time advance with the ADI method. Variable time stepping with a fixed Courant–Friedrichs–Lewy (CFL) number 0.5 is used. Time steps are of the order of 10^{-3}. One tidal cycle takes approximately 70–90 CPU h.

2.3. Pressure Poisson equation

The fractional step method used here leads to the following Poisson equation for the pressure correction,

$$\frac{\partial}{\partial\xi_i}\left(G^{ij}\frac{\partial\phi^{n+1}}{\partial\xi_j}\right) = \frac{\partial U_j^{c(n)}}{\partial\xi_j}\,. \tag{2.17}$$

Here $U_j^{c(n)} = J^{-1}(\partial\xi_j/\partial x_i)u_i^{(n)}$ is an intermediate volume flux and superscripts $n, n+1$ denote current and advanced time level. Finally, velocity and pressure are corrected as

$$U_j^{c(n+1)} = U_j^{c(n)} - G^{jm}\frac{\partial\phi^{n+1}}{\partial\xi_m}, \tag{2.18}$$

$$p^{*(n+1)} = p^{*(n)} + C_1\phi^{n+1}. \tag{2.19}$$

Here C_1 is a factor that depends on the time step in the Runge–Kutta substep. Equation (2.17) is solved by a two-dimensional multigrid method developed by

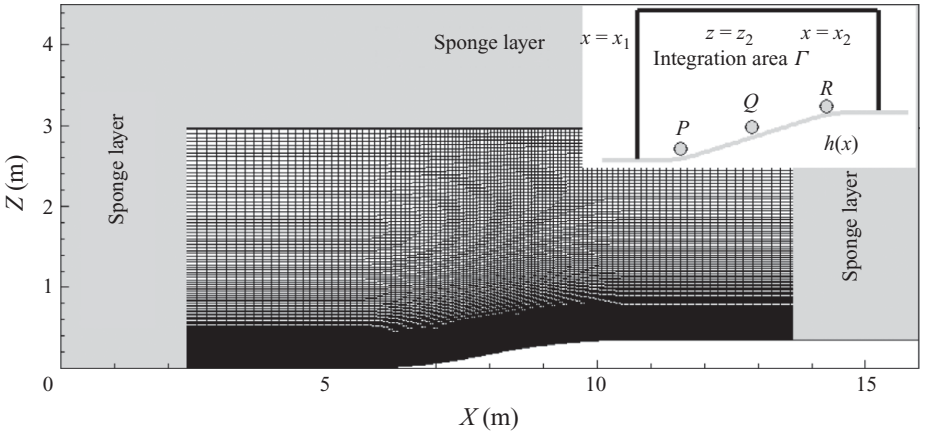

FIGURE 4. Curvilinear grid in the computational domain for case 2. A sponge layer surrounds the domain on the left, right and top. The inset shows an area Γ demarcated on the top by the line $z = z_2$, on the left by $x = x_1$, on the right by $x = x_2$, on the bottom by $z = h(x)$. Quantities integrated over the area Γ will be used to quantify turbulence and internal waves at the slope. In the inset, three points on the slope are shown: Q at the middle, and P and R at opposite edges of the slope.

Zeeuw (1990) and based on sawtooth multigrid cycling (i.e. one smoothing sweep after each coarse grid correction) with smoothing by incomplete line LU decomposition, weighted nine-point prolongation and restriction, and Galerkin approximation of coarse grid matrices.

2.4. *Boundary condition*

Periodicity is imposed in the spanwise ($\zeta = \zeta(y)$) direction on velocity, density ρ^* and pressure, p^*.

The bottom boundary, $\eta = 0$, has zero velocity and zero temperature gradient. Grids are forced to be orthogonal near the boundary so that

$$\frac{\partial \rho}{\partial \eta} = 0 \Rightarrow \frac{\partial \rho^*}{\partial \eta} = \cos(\beta) \quad \text{at} \quad \eta = 0\,, \tag{2.20}$$

where $\beta = \tan^{-1}(h_x)$. At the top of the domain, $\partial u/\partial \eta = 0, v, w = 0$ and $\rho^* = 0$. On the left and right sides, $\partial u/\partial \xi = 0, v, w = 0$ and $\rho^* = 0$. To match the boundary condition for the density deviation, ρ^*, between the left and the bottom (similarly, the right and the bottom) boundaries, $\partial \rho^*/\partial \eta$ is set to zero on both the left and right ends of the bottom boundary, then it gradually reaches the value given by (2.20) within 1 m from the both ends and it is fixed at this value for the remaining extent of the bottom boundary. The pressure boundary conditions are $\partial p^*/\partial \eta = 0$ at the bottom and top walls and $p^* = 0$ on the left and right of the computational domain.

Rayleigh damping or a 'sponge' layer is used on the left, right and top boundaries of the computational domain as shown in figure 4 so as to minimize spurious reflections from the artificial boundary into the 'test' section of the computational domain. The velocity and scalar fields are relaxed towards the background state in the sponge region by adding damping functions $-\sigma(\xi, \eta)[u_i(\boldsymbol{x}, t) - 0]$ $(i = 2, 3)$ and $-\sigma(\xi, \eta)[\rho^*(\boldsymbol{x}, t) - 0]$ to the right-hand side of the momentum and scalar equations, respectively. The value of $\sigma(\xi, \eta)$ is zero everywhere except in a region close to the top, left and right boundaries where it increases exponentially and reaches a maximum

value corresponding to $2\sigma(\xi, \eta)\Delta t \sim O(1)$ where Δt is the time step of the simulation. Since $\Delta t \sim O(10^{-3})$, it follows that $\sigma(\xi, \eta) \sim O(500)$.

2.5. *Subgrid-scale model*

The dynamic eddy-viscosity model (Zang, Street & Koseff 1993; Vreman, Geurts & Kuerten 1997) is used for the SGS stress tensor, $\boldsymbol{\tau}$. The SGS heat flux, $\boldsymbol{\lambda}$, is obtained using a dynamic eddy-diffusivity model (Armenio & Sarkar 2002). The expressions for the SGS models are as follows:

$$\tau_{ij} = -2\nu_T \overline{S_{ij}}, \qquad \nu_T = C\overline{\Delta}^2 |\overline{\boldsymbol{S}}| \tag{2.21}$$

and

$$\lambda_j = -\kappa_T \frac{\partial \overline{\rho^*}}{\partial x_j}, \qquad \kappa_T = C_{\rho^*} \overline{\Delta}^2 |\overline{\boldsymbol{S}}|\,. \tag{2.22}$$

Here, C and C_{ρ^*} are the Smagorinsky coefficients evaluated through a dynamic procedure introduced by Germano *et al.* (1991). Averaging over the spanwise direction is employed to prevent excessive back scattering owing to large local fluctuations. The dynamic procedure involves the introduction of an additional test filter denoted by $\widehat{(\cdot)}$. The model coefficient, C, in the SGS stress model is given by

$$C = \frac{\langle M_{ij} L_{ij} \rangle}{\langle M_{kl} M_{kl} \rangle}, \tag{2.23}$$

where

$$L_{ij} = \widehat{\overline{u}_i \overline{u}_j} - \widehat{\overline{u}}_i \widehat{\overline{u}}_j, \quad M_{ij} = 2\widehat{\overline{\Delta}^2 |\overline{\boldsymbol{S}}|} \overline{S}_{ij} - 2\widehat{\overline{\Delta}}^2 |\widehat{\overline{\boldsymbol{S}}}| \widehat{\overline{S}}_{ij}, \tag{2.24}$$

The model coefficient, C_{ρ^*}, in the SGS heat-flux model is given by

$$C_{\rho^*} = \frac{\langle M_i^{\rho^*} L_i^{\rho^*} \rangle}{\langle M_j^{\rho^*} M_j^{\rho^*} \rangle}, \tag{2.25}$$

where

$$L_i^{\rho^*} = \widehat{\overline{\rho^* \overline{u}_i}} - \widehat{\overline{\rho^*}} \widehat{\overline{u}_i}, \quad M_i^{\rho^*} = 2\widehat{\overline{\Delta}^2 |\overline{\boldsymbol{S}}|} \frac{\partial \overline{\rho^*}}{\partial x_i} - 2\widehat{\overline{\Delta}}^2 |\widehat{\overline{\boldsymbol{S}}}| \frac{\partial \widehat{\overline{\rho^*}}}{\partial x_i}. \tag{2.26}$$

The test filter, denoted by $\widehat{(\cdot)}$, and the grid filter, denoted by $\overline{(\cdot)}$, are applied over only the spanwise direction using a trapezoidal interpolation rule. For instance, application of the explicit filters to an LES variable, $\overline{\Psi}_i$, at node i is given by

$$\widehat{\overline{\Psi}}_i = \tfrac{1}{4}\left[\overline{\Psi}_{i-1} + 2\overline{\Psi}_i + \overline{\Psi}_{i+1}\right], \tag{2.27}$$

$$\overline{\overline{\Psi}}_i = \tfrac{1}{8}\left[\overline{\Psi}_{i-1} + 6\overline{\Psi}_i + \overline{\Psi}_{i+1}\right]. \tag{2.28}$$

The filter width ratio $\widehat{\overline{\Delta}}/\overline{\Delta}$ is taken as $\sqrt{6}$, recommended by Lund (1997) to be the optimal choice for filters evaluated using the trapezoidal rule.

2.6. *Domain resolution and initialization*

The computational domain length in the horizontal directions is given by l_x and l_y. The vertical domain length is l_z. Five different numerical experiments are performed in a parametric study on the influence of slope length, l, as shown in tables 1–2. Cases 1 and 2 are DNS with $\Delta x^+_{min} \leqslant 20$, $\Delta y^+ \leqslant 10$ and $\Delta z^+_{min} \leqslant 2$ in terms of the viscous wall unit ν/u_τ. Cases 3–5 correspond to a resolved-LES mode with a dynamic eddy-viscosity model.

Case	U_0 (m s^{-1})	N_∞^2 (s^{-2})	Ω^2 (s^{-2})	ν (m^2 s^{-1})	l (m)	l_x (m)	l_y (m)	l_z (m)	Remark
1	0.125	131.6	1.0	10^{-6}	1.7	!8	1	3	DNS
2	0.125	131.6	1.0	10^{-6}	3.5	10	1	3	DNS
3	0.125	131.6	1.0	10^{-6}	7.2	15	1	3	LES
4	0.125	131.6	1.0	10^{-6}	12.0	30	1	3.5	LES
5	0.125	131.6	1.0	10^{-6}	25.0	60	1	5.5	LES

TABLE 1. Dimensional parameters of the simulated cases.

Case	Re_s	$\frac{\Omega^2}{N_\infty^2}$	Pr	$Ex = U_0/\Omega l$	ϵ	N_x	N_y	N_z	Δx^+_{min}	Δy^+	Δz^+_{min}
1	177	0.0076	1.0	0.0735	1.0	260	256	260	15	7.5	1.4
2	177	0.0076	1.0	0.0357	1.0	260	256	260	20	10	2.0
3	177	0.0076	1.0	0.01736	1.0	260	256	260	40	25	2.3
4	177	0.0076	1.0	0.0104	1.0	800	256	260	60	50	2.6
5	177	0.0076	1.0	0.005	1.0	600	256	260	100	60	3.0

TABLE 2. Non-dimensional parameters and grid resolution of the simulated cases. The excursion number is chosen to be small, as is typical for deep water topography, and the slope angle is critical.

The flow is statistically homogeneous in the spanwise direction and a y-average is used to compute the time-dependent mean, $\langle \mathscr{A} \rangle_y(x, z, t)$, as follows:

$$\langle \mathscr{A} \rangle_y(x, z, t) = \frac{1}{l_y} \int_0^{l_y} \mathscr{A}(x, y, z, t)\, \mathrm{d}y. \tag{2.29}$$

2.7. *Selection of simulated cases*

Table 1 gives the dimensional parameters of the simulations. The non-dimensional parameters in table 2 show that each case is near-critical ($\epsilon \sim 1$) and has a low excursion number. These non-dimensional parameters can be compared with an oceanic example of tidal flow over sloping topography in deep water: a tidal amplitude of $U_0 = 0.025\,\mathrm{m\,s^{-1}}$, a tidal frequency of $\Omega = 1.4 \times 10^{-4}\,\mathrm{rad\,s^{-1}}$ corresponding to the M_2 tidal period of 12.4 h, a low latitude with $f = 3.5 \times 10^{-5}\,\mathrm{rad\,s^{-1}}$, and $N_\infty = 1\,\mathrm{cph} = 1.74 \times 10^{-3}\,\mathrm{rad\,s^{-1}}$. A representative slope length of 5 km leads to an excursion number of 0.04. In the simulations, Ex is below this value, except in case 1 where $Ex = 0.0735$. The critical slope angle $\beta = 5^\circ$ is in the range $\beta = 4^\circ$–5°, typical of the ocean. The Stokes–Reynolds number, $Re_s = 177$, of the simulated cases is smaller than the value of $Re_s = 2975$ in the oceanic example but still sufficiently large in the case of critical slope to exhibit turbulence, owing to a substantial increase in near-bottom velocity, as will be demonstrated. Note that dimensional variables are solved. However, for simplicity of notation, we will drop subscript d when presenting results in the following section.

3. Velocity field

The baroclinic response at a near-critical slope results in intensification of the near-bottom velocity. In the following discussion, 'across-slope' velocity denoted by U_{sl} refers to the slope-parallel velocity pointing in the ξ-direction.

The time evolution of the across-slope velocity at a point Q, adjacent to the slope midpoint, is shown in figure 5(a). As this location is very close to the slope,

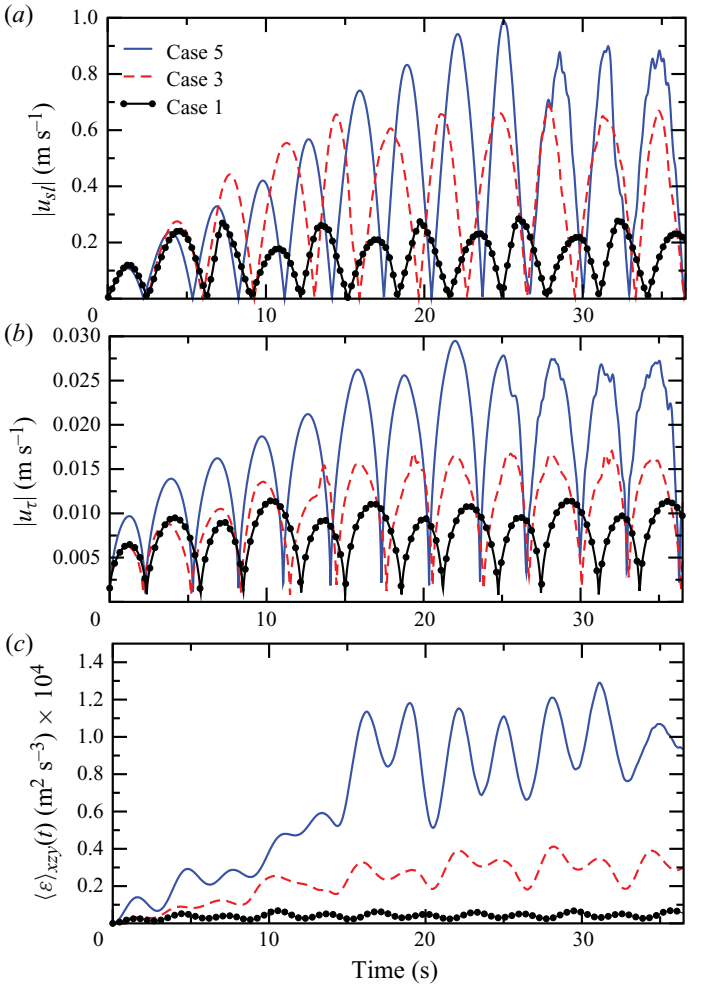

FIGURE 5. (Colour online) Time evolution of (*a*) the along-slope velocity U_{sl} and (*b*) the magnitude of friction velocity $|u_\tau|$, at a particular location which is inside the boundary layer at the midpoint of the slope denoted by point Q in the inset of figure 4 for different cases. (*c*) Viscous dissipation calculated as an average over the region Γ in the inset in figure 4.

the mean flow velocity is predominantly parallel to the slope of the topography. Initially, the amplitude of the near-bottom velocity increases rapidly with time due to resonant buoyant forcing. Nonlinear effects become important and there is a transition to turbulence as discussed by Gayen & Sarkar (2010). Shortly after, viscous dissipation becomes important and leads to amplitude saturation. After a couple of initial cycles, the flow field achieves a quasi-steady state where the variation of the velocity amplitude is slight. By increasing the slope length, the resonance area increases, resulting in enhancement of the baroclinic tidal velocity response in case 5 ($l = 25$ m) relative to case 1 ($l = 1.7$ m). However, longer slopes require more time to adjust between the higher resonant forcing and frictional force before reaching a quasi-steady state. Here, case 5 requires five tidal cycles compared to three and two cycles for the smaller domains in cases 3 and 1, respectively.

Case	$u_{\tau,max}$	$u_{\tau,avg}$	$c_{f,max}$	$c_{f,avg}$	$\frac{\tau_{w,max}}{(1/2)\rho_0 U_{sl,max}^2}$
1	0.010	0.0077	0.0128	0.0076	0.00320
2	0.012	0.0090	0.0184	0.0103	0.00180
3	0.015	0.0104	0.0284	0.0138	0.00148
4	0.023	0.0119	0.0504	0.0181	0.00122
5	0.025	0.0130	0.0556	0.0202	0.00118

TABLE 3. Comparison of the overall boundary properties between cases. Here, u_τ is the friction velocity calculated based on the wall friction, τ_w, and c_f is the friction coefficient. The subscript *avg* denotes an average over at least five complete tidal cycles and *max* denotes the amplitude of the oscillatory wall stress, calculated as an average of the peak values of the cycle.

Two measures of frictional effects are shown: (i) frictional velocity u_τ at point Q in figure 5(b) and (ii) viscous dissipation $\langle\varepsilon\rangle_{xyz}(t)$, calculated as an average over an area Γ adjacent to the slope, in figure 5(c). Here, the friction velocity is calculated based on the wall friction, τ_w,

$$u_\tau = \sqrt{\frac{\tau_w}{\rho_0}}, \quad \tau_w = \rho_0 \nu \left[\left(\frac{\partial \langle w \rangle_y}{\partial x} \right)^2 + \left(\frac{\partial \langle u \rangle_y}{\partial z} \right)^2 + \left(\frac{\partial \langle v \rangle_y}{\partial x} \right)^2 + \left(\frac{\partial \langle v \rangle_y}{\partial z} \right)^2 \right]_{at\ bottom}^{1/2}. \tag{3.1}$$

The term

$$\langle\varepsilon\rangle_{xyz}(t) = \nu \left\langle \frac{\partial u_i}{\partial x_j} \frac{\partial u_i}{\partial x_j} \right\rangle_{xyz} \tag{3.2}$$

is viscous dissipation (more accurately pseudo-dissipation) and includes both mean and turbulent velocities. Both quantities exhibit a rapid increase during an initial transient followed by an approximately quasi-steady stage.

Time-averaged quantities for different cases are calculated based on quasi-steady-state data. Temporally averaged amplitude and time-averaged frictional velocity for different cases are tabulated in table 3. Both statistics increase monotonically with slope length. The friction coefficients based on average wall friction and maximum wall friction velocity are calculated by

$$c_{f,avg} = \frac{u_{\tau,avg}^2}{(1/2)U_0^2}, \quad c_{f,max} = \frac{u_{\tau,max}^2}{(1/2)U_0^2}, \tag{3.3}$$

and also exhibit an increase with increasing slope length. If $U_{sl,max}$ is chosen to calculate friction factor instead of U_0, its behaviour shows a reverse trend of a decrease with increasing slope length. In this context, it is worth noting that the local Reynolds number increases with slope length. Therefore, the reverse trend is similar to the well-known decrease in the value of c_f with increasing Re in a turbulent flow.

Profiles of $U_{sl}(z_p, \phi)$ are shown in figures 6(a) and 6(b) at $\phi = 0°$ and $\phi = 180°$, respectively. In all cases, velocities in the bottom boundary layer are significantly larger compared to the external (barotropic) current. There is a 90° phase lead of the baroclinic response with respect to the barotropic current. Velocity profiles become fuller with increasing slope length. The velocity profile has a spatial oscillation that is associated with internal wave modes. Figure 6(c) shows non-dimensional velocity profiles during maximal upslope flow using the following quantities for normalization: the maximal amplitude, U_{sl}^{max}, over the velocity profile and the beam width, l_b, defined as the distance from the bottom of the profile in figure 6(a) up to the height where

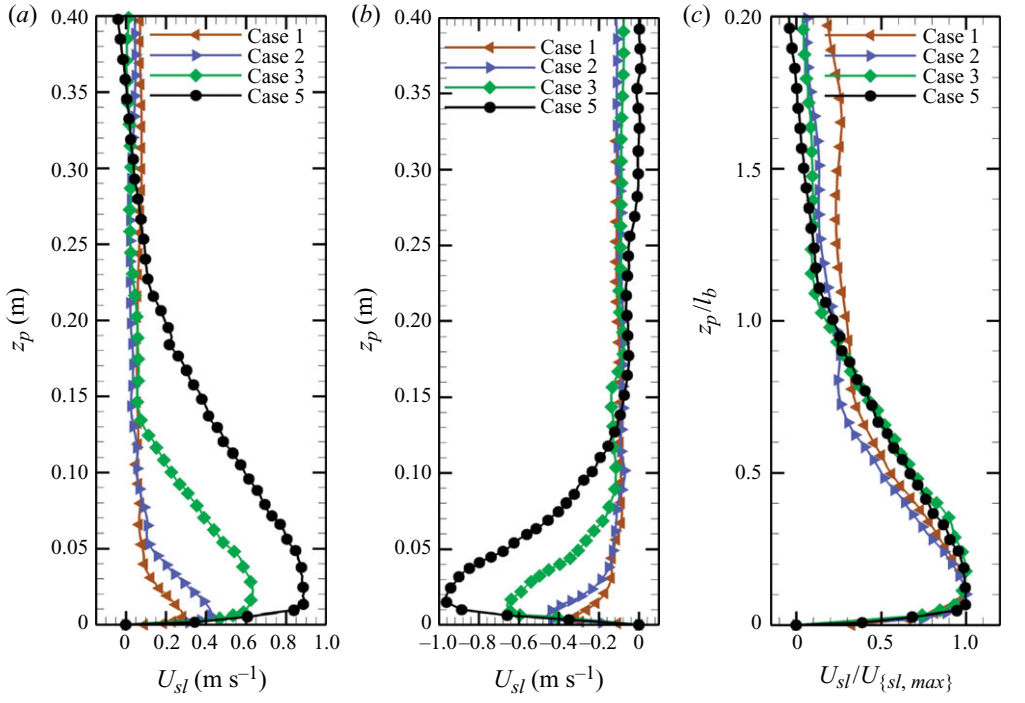

FIGURE 6. (Colour online) Profiles of velocity as a function of the wall-normal distance at the midpoint of the slope for (*a*) $\phi = 0°$ and (*b*) $\phi = 180°$. (*c*) Profiles at $\phi = 0°$ replotted after normalization with the maximal velocity amplitude, U_{sl}^{max}, and the beam width, l_b.

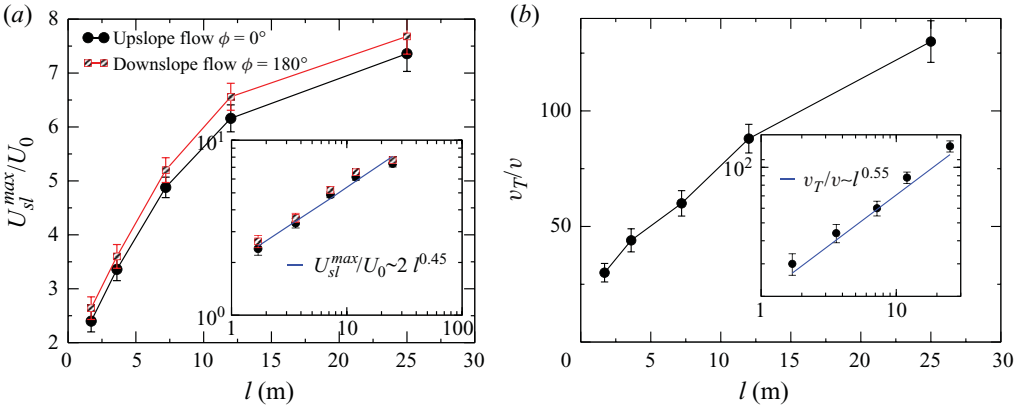

FIGURE 7. (Colour online) (*a*) Amplitude of the along-slope velocity as a function of the slope length. The inset is a replot of the data in log–log scale along with a linear least-squares fit. (*b*) Turbulent viscosity normalized by molecular viscosity is shown as a function of the slope length. The inset is a replot in log–log scale.

the velocity is 15% of U_{sl}^{max}. The profiles for the different cases tend to collapse into a single curve.

The maximal velocity amplitude, U_{sl}^{max}, increases with slope length as shown in figure 7(*a*). The maximal downslope velocity amplitude is somewhat larger than the corresponding upslope value for all cases. In the inset of figure 7(*a*), U_{sl}^{max} is shown

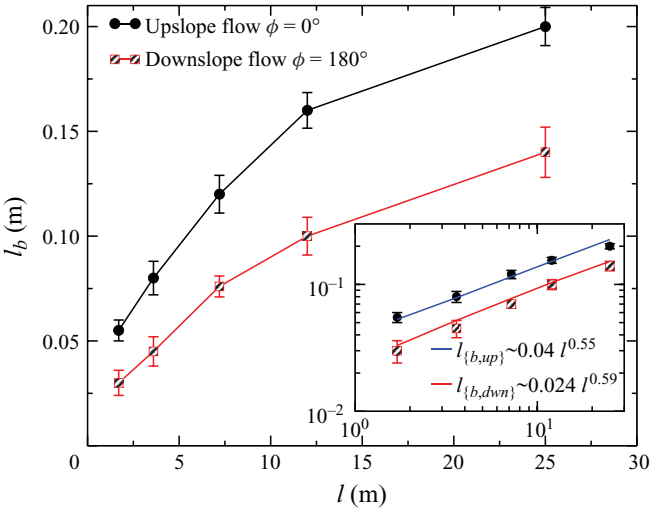

FIGURE 8. (Colour online) Jet width, l_b, as a function of the horizontal slope length is shown for both upslope and downslope boundary flows. Inset shows data replotted in log–log scale along with its linear least-squares fit.

as a function of slope length in a log–log plot. The linear fit in the inset shows that $U_{sl}^{max} \simeq l^{0.45}$. In an earlier experiment, Zhang *et al.* (2008) found a different scaling law of $U_{sl}^{max} \simeq l^{2/3}$ in the regime of laminar flow. Zhang *et al.* (2008) were able to provide theoretical justification based on an analytical result obtained by Dauxois & Young (1999) for a laminar oscillatory boundary layer:

$$\frac{U_{sl}^{max}}{U_0} \sim \frac{\Omega}{N_\infty}\left[\frac{\sqrt{N_\infty^2 - \Omega^2}}{\nu}\right]^{1/3} l^{2/3}. \tag{3.4}$$

As a first approximation, the analysis can be extended to turbulent flow by replacing ν in (3.4) by $\nu_{tot} = \nu + \nu_T$ and $\nu_T = -\langle u'w'\rangle / \mathrm{d}\langle u\rangle/\mathrm{d}z$ taken to be independent of z. The height-averaged value of ν_T is calculated at midslope from the simulation data and plotted in figure 7(b) to find the dependence of ν_T on slope length. In the inset of figure 7(b), ν_T/ν is replotted as a function of the slope length in log–log scale and the linear fit suggests that ν_T scales as $l^{0.55}$. Therefore, (3.4) extended to the turbulent regime becomes

$$\left.\begin{aligned} &\frac{U_{sl}^{max}}{U_0} \sim \frac{\Omega}{N_\infty}\left[\frac{\sqrt{N_\infty^2 - \Omega^2}}{\nu_T + \nu}\right]^{1/3} l^{2/3} \\ \Rightarrow\ &\frac{U_{sl}^{max}}{U_0} \sim \frac{\Omega}{N_\infty}\left[\frac{\sqrt{N_\infty^2 - \Omega^2}}{\nu_T}\right]^{1/3} l^{2/3} \quad \text{as } \nu_T > 10\nu \\ \Rightarrow\ &\frac{U_{sl}^{max}}{U_0} \sim \frac{\Omega}{N_\infty}\left[N_\infty^2 - \Omega^2\right]^{1/6} l^{0.48}. \end{aligned}\right\} \tag{3.5}$$

The dependence on l in (3.5) is quite close to the relation, $U_{sl}^{max} \sim l^{0.45}$, inferred previously by a direct fit to the simulation data.

The beam width, l_b, plotted in figure 8 exhibits a monotonic increase with increasing slope length. The beam width in the case of the upslope flow is larger than in the downslope flow for all five cases. The inset in the figure shows power-law fits to the dependence of beam width on slope length.

The full velocity field computed in the simulation can be decomposed as

$$\boldsymbol{u}(\boldsymbol{x}, t) = \boldsymbol{u}_{ba}(x, z, t) + \boldsymbol{u}_{bc}(\boldsymbol{x}, t), \tag{3.6}$$

where $\boldsymbol{u}_{ba}$ and $\boldsymbol{u}_{bc}(\boldsymbol{x}, t)$ are respectively barotropic and baroclinic responses. The decomposition of the velocity is based on Nash *et al.* (2004, 2006), as further discussed in the Appendix. The baroclinic velocity $\boldsymbol{u}_{bc}(\boldsymbol{x}, t)$ is further decomposed into a mean wave velocity $\langle u_{bc}\rangle_y(x, z, t)$ obtained by a spanwise average, and a turbulent fluctuation $\boldsymbol{u}'(\boldsymbol{x}, t)$ with respect to the mean.

The baroclinic streamwise velocity can be approximated by a sinusoidal form

$$\langle u_{bc}\rangle_y(x, z, t) = u_0(x, z)\sin(\Omega t + \Delta\phi_u(x, z)) \tag{3.7}$$

with a space-dependent amplitude $u_0(x, z)$ and the space-dependent phase, $\Delta\phi_u(x, z)$, with respect to the background barotropic tidal flow. The parameters $u_0(x, z)$ and $\Delta\phi_u(x, z)$, determined by a least-squares method from the time series data taken over six cycles, are shown in figures 9(*a*) and 9(*b*), respectively, for case 4. The amplitude distribution illustrates internal wave beam strength and spatial structure. The region with high amplitude adjacent to the slope corresponds to a narrow and strong internal wave beam. The amplitude increases to $\sim 0.81\,\mathrm{m\,s^{-1}}$ at the slope and remains relatively constant at the slope. When the beam travels away from its generation zone (along the slope) into the fluid, it gradually widens and weakens. At a particular position in the centre of the beam, 1 m away from the right edge of the topography slope, the amplitude decreases to $0.45\,\mathrm{m\,s^{-1}}$. The spreading of the wave beam is caused by viscous diffusion and also by dispersion since waves with smaller wavelength and, therefore, lower phase velocity may be locally dissipated, leaving larger wavelength modes in the propagating wave. The spreading of the wave beam is also observed in observations at Kaena Ridge, Hawaii, by Nash *et al.* (2006) and from a model topography in a laboratory experiment by Echeverri *et al.* (2009).

Figure 9(*b*) shows that the oscillatory velocity exhibits significant spatial variability in the phase, ϕ, with respect to the barotropic tidal velocity. There is phase variation along the sloping boundary associated with internal wave propagation. As shown in § 5, the internal wave flux associated with the beam is such that the energy propagation is outward from the sloping topography. There is also an area of recirculation between the lower edge of the beam and the flat top of the topography. Other simulated cases also show similar spatial variability of phase and amplitude.

4. Thermal bore

The baroclinic wave response is intensified at a region of critical slope and leads to energy concentration into a beam as discussed in the previous section. An upslope-moving tidal bore or bolus may also form, as observed by Lim *et al.* (2010) in laboratory experiments of internal tide generation. In the problem of reflection at a critical slope, the upslope propagation of a thermal front has been observed in the laboratory (Thorpe 1992), and the upslope propagation of a bolus and on to the shelf has been identified in simulations (Venayagamoorthy & Fringer 2007). In the present simulations of the generation problem, we find that an upslope bore results as a part of the baroclinic response. The thermal front has sufficient energy to move rightwards as a gravity current along the top horizontal portion of the topography into the stable stratified region. Using a three-dimensional visualization of a density iso-surface, the on-slope propagation of the thermal front is shown in figure 10. The thermal front is unstable and undergoes spanwise corrugations as shown in figure 10(*b*). This is similar

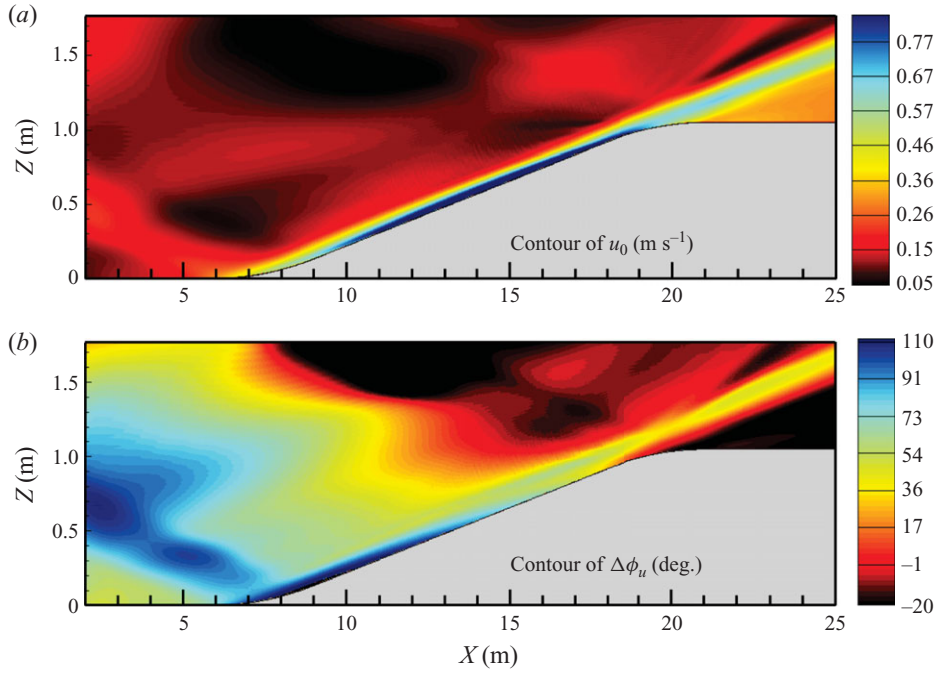

FIGURE 9. (*a*) Baroclinic velocity amplitude $u_0(x, z)$ and (*b*) phase $\Delta\phi_u(x, z)$ as a function of the space given in (3.7) for case 4.

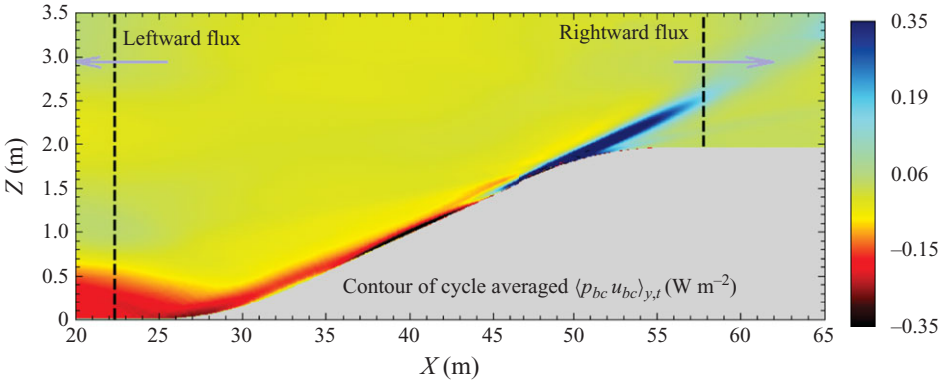

FIGURE 15. Spatial distribution of the cycle-averaged streamwise internal wave flux, $\langle f^{\parallel}\rangle = \langle p_{bc}u_{bc}\rangle_{y,t}$ (W m^{-2}) is shown in the x–z plane for case 5. Time averaging is performed over the final five cycles of the simulation. Here, the vertical dashed lines given by $x = x_1$ and $x = x_2$ from the left indicate the vertical integration boundaries used for obtaining the net streamwise flux.

to the classical lobe and cleft instability found in the case of gravity currents. Finally, isolated fluid patches detach from the on-slope-propagating turbulent bore/bolus as shown in figure 10(*c*, *d*) and dissipate locally due to the combined effect of turbulent and molecular diffusions.

5. Wave energetics

A complex wave pattern containing an energetic beam and internal waves with a wide range of phase angles emerges as shown by Gayen & Sarkar (2010). Here, we

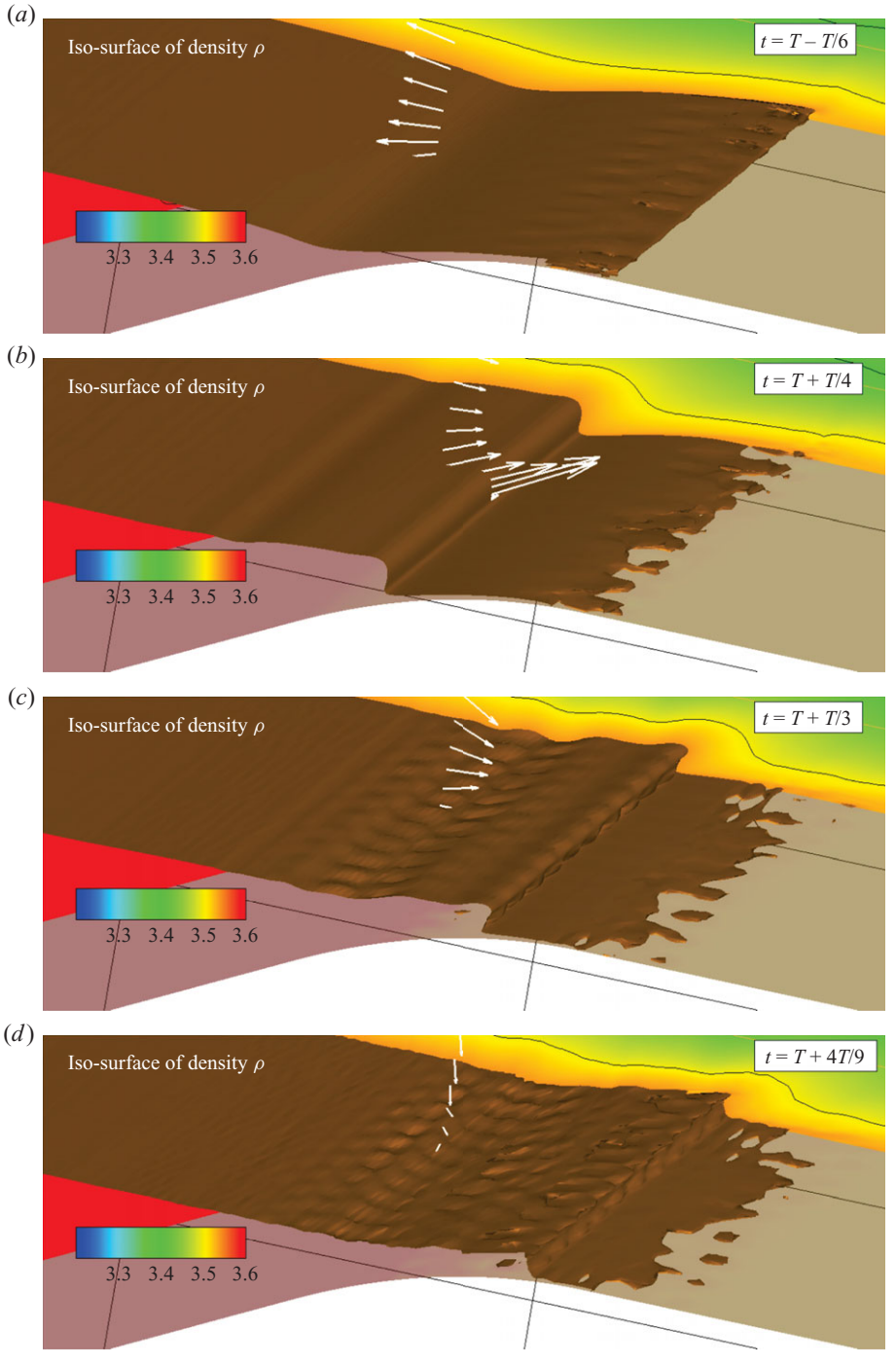

FIGURE 10. (*a–d*) Formation and propagation of the thermal bore shown at four different time instants. The velocity vectors, taken along a vertical line at a point R in the inset of figure 4, are shown by arrows. Here, the colour scale refers to contour value of total density with an arbitrary reference value.

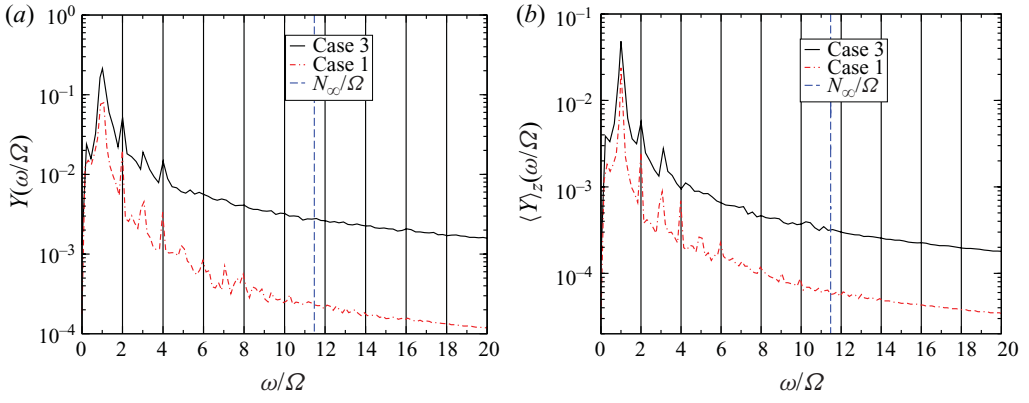

FIGURE 11. (Colour online) (*a*) Power spectra, Y, based on the time-series data of the baroclinic streamwise velocity at a location midway on the slope (point Q in the inset of figure 4) and inside the boundary layer for cases 1 and 3. The time series is taken over eight cycles and the spectra are averaged over the spanwise direction. The line average of the power spectra, $\langle Y\rangle_z$, is shown in (*b*). The dashed vertical line corresponds to the normalized buoyancy frequency.

quantify the energy transport including the contribution of higher harmonics relative to the fundamental, i.e. the frequency of the barotropic tidal forcing.

The baroclinic streamwise velocity field over an area containing the slope of the topography is subjected to spectral analysis. In figure 11(*a*), the power spectrum at a location Q, midway on the slope and close to the bottom, is shown for cases 1 and 3. The spectra show energy at several temporal harmonics ($n\Omega, n \in \mathbb{N}$), subharmonics $\omega \in [0, \Omega)$ and interharmonics ($\omega_\alpha + n\Omega, \omega_\alpha \in [0, \Omega)$). In figure 11(*a*), the discrete spectral peak at the barotropic tidal frequency, Ω, corresponds to an energetic linear response which, in physical space, corresponds to the strong beam parallel to the slope in figure 2. The spectrum shows discrete peaks at the second and third harmonics as well as significant strength at frequencies $\omega > N_\infty$. The energy content at harmonics, interharmonics and subharmonics is higher for larger slope lengths. Significantly, larger amplitude of the continuous part of the spectrum (especially at high frequencies) is observed at the longer slope length of case 3 relative to case 1. The continuous spectrum is associated with nonlinear interactions and, at high frequencies, reflects the broadband multiscale nature of turbulence. With increasing slope length, turbulence (quantified in the next section) is enhanced due to the increase in the boundary velocity. Therefore, the relative magnitude of the continuous spectrum increases with increasing slope length. The power spectra averaged over a vertical line at location Q, defined in the inset of figure 4, are shown in figure 11(*b*) for both cases. The line extends from bottom of the wall to the height of the control area Γ so that the averaging procedure includes points both inside and outside the boundary layer. The discrete peaks at the higher harmonics and the interharmonics are also present in the averaged spectrum.

To illustrate the shift from turbulence inside the boundary layer to internal waves propagating outside, we choose three locations (a–c) at different heights on a vertical line at point Q midway on the slope. Position (a) (height with respect to the bottom, $z^* = 0.01$ m) is well inside the boundary layer, position (b) ($z^* = 0.15$ m) is outside the boundary layer and position (c) ($z^* = 0.4$ m) is well outside. Power spectra of the baroclinic velocity field at those locations are shown in figure 12(*a*). For all positions, the global spectral peak occurs at the fundamental tidal frequency. Because

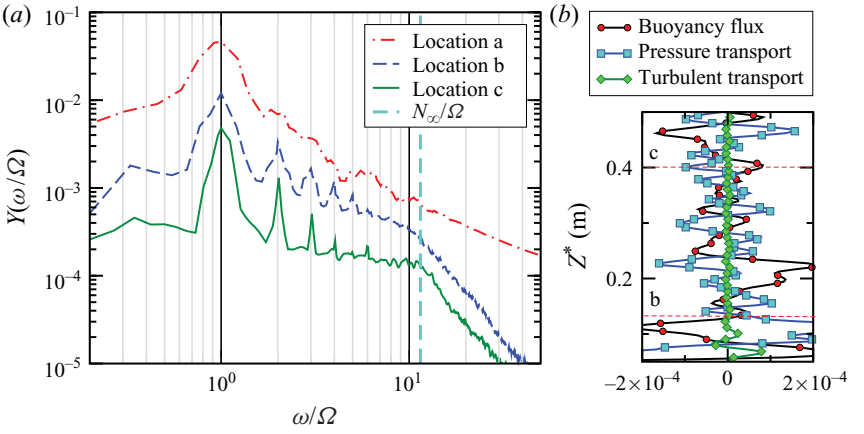

FIGURE 12. (Colour online) (*a*) Power spectra of the baroclinic velocity field at locations (a), (b) and (c) along a vertical line at point Q in the inset of figure 4 for case 1. The time series is taken over eight cycles. (*b*) Profile of buoyancy flux, pressure transport and turbulent transport as a function height above the bottom at location Q. Data are taken at $\phi = 0°$.

of strong turbulence activity, position (a) located inside the boundary layer has a continuous spectrum of significant magnitude that obscures discrete peaks at harmonics of the tidal frequency. Positions (b) and (c) are external to the boundary layer and are locations with little turbulence. Nevertheless, there is a significant continuous spectrum. Boundary-layer turbulence on a non-sloping bottom generates an externally propagating wave field without discrete peaks, as shown in our previous work on a steady boundary layer (Taylor & Sarkar 2007) and an oscillating boundary layer (Gayen *et al.* 2010). Such turbulence-generated waves and, in addition, wave–wave interactions of the topography-generated waves lead to a continuous spectrum at points (b) and (c) in the present problem. It is worth noting that there is a sharp decay in the amplitude of frequencies larger than the buoyancy frequency, N_∞, at points (b) and (c) since the background does not support freely propagating waves with $\omega > N_\infty$. Also, at locations (b) and (c) the peaks at the tidal harmonics increase in strength relative to the continuous part of the spectrum. This is probably because the continuous spectrum is associated with smaller length-scale waves that suffer higher viscous dissipation. Profiles of buoyancy flux, pressure transport and turbulent transport are plotted in figure 12(*b*) at maximal upslope flow. The location of observation points (b) and (c) are shown in the same figure by dashed horizontal lines. At these locations, buoyancy flux and pressure transport dominate. Turbulent production and dissipation as well as turbulent transport are insignificant, confirming that there is little contribution of turbulence to fluctuations at points (b) and (c).

A comparative study of energy distribution among the harmonics is performed for different slope lengths. In figure 13(*a*), the line-averaged energy, $\langle Y \rangle_z$, is shown for the first three harmonics. For all cases, the fundamental dominates. The energy content at the higher harmonics decreases with increasing frequency. The energy at all harmonics increases with the slope length. The relative importance of the energy at higher harmonics with respect to the fundamental is shown as a function of the slope length in figure 13(*b*). For each case, the fundamental is assigned as 100% and the energy in other harmonics is expressed as a relative percentage. Energy contained in higher harmonics relative to the fundamental increases with increasing slope length. For example, the energy of the second harmonic in case 1 with slope length 1.7 m is

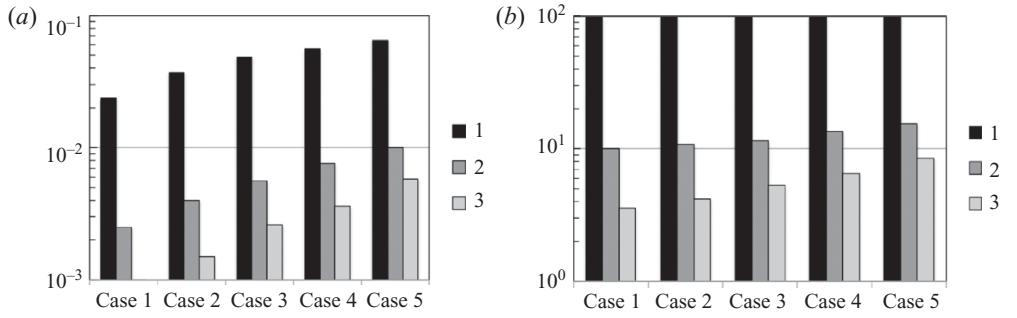

FIGURE 13. Energy distribution over harmonics 1–3 at a point on the slope and in the boundary layer is shown with absolute units ($m^2\,s^{-2}$) in the bar chart of (a). Bar 1 in black corresponds to the fundamental at the tidal frequency. Bars 2 and 3 shown in dark grey and light grey, respectively, correspond to the second and third harmonics. Plot (b) is the same as (a) except that all quantities are in relative units.

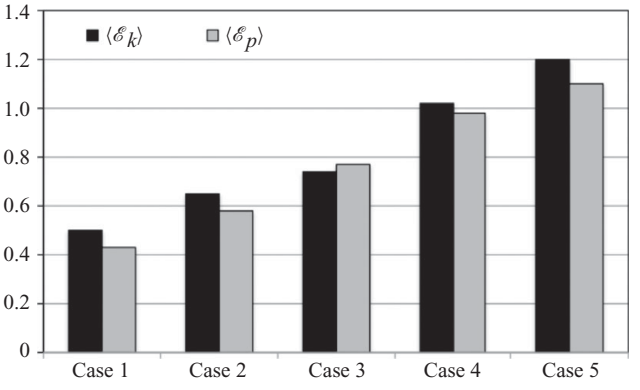

FIGURE 14. Normalized area-integrated kinetic energy density, $\langle \mathscr{E}_k \rangle$, and potential energy density, $\langle \mathscr{E}_p \rangle$, are shown as a function of the slope length. Normalization factor is $(1/2)\rho_0 U_0^2 \Gamma$.

10% of the energy at the fundamental, a value that increases to 15% for the largest slope length of 25 m in case 5.

The energy density, E_{IW}, in the internal wave field is decomposed into kinetic energy, E_k, and potential energy, E_p, as follows:

$$E_k = \tfrac{1}{2}\rho_0\big(\langle u_{bc}\rangle_y^2 + \langle v_{bc}\rangle_y^2 + \langle w_{bc}\rangle_y^2\big), \tag{5.1}$$

$$E_p = \frac{g^2\langle \rho_{bc}\rangle_y^2}{2\rho_0 N_\infty^2}. \tag{5.2}$$

We choose an area Γ containing the topography and a time record of length nT, where T is the time period of a tidal cycle and $n = 5$. The energies in this space–time section are normalized as follows:

$$\langle \mathscr{E}_k \rangle = \frac{1}{nT\Gamma U_0^2}\int_{nT}\int_{\Gamma}\big(\langle u_{bc}\rangle_y^2 + \langle v_{bc}\rangle_y^2 + \langle w_{bc}\rangle_y^2\big)\,\mathrm{d}A\,\mathrm{d}t, \tag{5.3}$$

$$\langle \mathscr{E}_p \rangle = \frac{1}{nT\Gamma U_0^2}\int_{nT}\int_{\Gamma}\frac{g^2\langle \rho_{bc}\rangle_y^2}{\rho_0^2 N_\infty^2}\,\mathrm{d}A\,\mathrm{d}t. \tag{5.4}$$

The values of $\langle \mathscr{E}_k \rangle$ and $\langle \mathscr{E}_p \rangle$ for different cases are shown in figure 14. In most cases, the kinetic energy is greater than the potential energy. In a linear plane wave,

energy is equipartitioned between the kinetic and potential modes. In more general situations, there can be deviations from linear theory as in the viscous, nonlinear waves simulated in the present work.

Streamwise and vertical wave fluxes are defined by $f^{\parallel} = \langle p_{bc} u_{bc} \rangle_y$ and $f^{\perp} = \langle p_{bc} w_{bc} \rangle_y$, respectively. Here p_{bc} is the pressure anomaly calculated in the Appendix. Now spanwise-averaged total energy equation for a plane internal wave can be written in linearized form

$$\frac{\partial (E_k + E_p)}{\partial t} + U(x) \sin(\Omega t) \frac{\partial (E_k + E_p)}{\partial x} = -\frac{\partial f^{\parallel}}{\partial x} - \frac{\partial f^{\perp}}{\partial z} + q(x, z), \tag{5.5}$$

where $q(x, z)$ is a source (sink) term. Equation (5.5) is integrated over the area Γ to give

$$\begin{aligned} \frac{\partial}{\partial t} \int_{\Gamma} [E_k + E_p] \, \mathrm{d}A = & - \int_{\Gamma} \left[U(x) \sin(\Omega t) \frac{\partial E_k + E_p}{\partial x} \right] \mathrm{d}A \\ & - \left[\int_{h(x_2)}^{z_2} f^{\parallel}|_{x_2} - \int_{h(x_1)}^{z_2} f^{\parallel}|_{x_1} \right] \mathrm{d}z - \int_{x_1}^{x_2} f^{\perp}|_{z_2} \, \mathrm{d}x \\ & + \int_{\Gamma} q(x, z) \, \mathrm{d}A. \end{aligned} \tag{5.6}$$

The integration area Γ is bounded on the top by the line $z = z_2$, on the left by $x = x_1$, on the right by $x = x_2$ and $z = h(x)$ on the bottom. After averaging (5.6) over a time span of length nT, where $n = 5$, transient terms vanish and it gives

$$0 = \langle G \rangle - \langle F \rangle^{\parallel} - \langle F \rangle^{\perp} + \langle Q \rangle, \tag{5.7}$$

where the cycle-averaged net horizontal flux, $\langle F \rangle^{\parallel}$ (the sum of the outward fluxes on the left and right boundaries of the integration area Γ), and the net vertical flux, $\langle F \rangle^{\perp}$ (the outward fluxes on the top boundary of the integration area Γ) are defined respectively by

$$\langle F^{\parallel} \rangle = \frac{1}{nT} \int_{nT} \left[\int_{h(x_2)}^{z_2} f^{\parallel}|_{x_2} - \int_{h(x_1)}^{z_2} f^{\parallel}|_{x_1} \right] \mathrm{d}z \, \mathrm{d}t, \tag{5.8}$$

$$\langle F^{\perp} \rangle = \frac{1}{nT} \int_{nT} \int_{x_1}^{x_2} f^{\perp}|_{z_2} \, \mathrm{d}x \, \mathrm{d}t. \tag{5.9}$$

After normalizing by $(\pi/4)\rho_0 U_0^2 h^2 N_\infty$ (a quantity that appears in the linear theory of conversion to internal tides), (5.7) is rewritten as

$$0 = \langle \mathscr{G} \rangle - \langle \mathscr{F}^{\parallel} \rangle - \langle \mathscr{F}^{\perp} \rangle + \langle \mathscr{Q} \rangle. \tag{5.10}$$

Here, normalized values are defined as follows:

$$\left.\begin{aligned} \langle \mathscr{G} \rangle &= \frac{4\langle G \rangle}{\pi \rho_0 U_0^2 h^2 N_\infty}, & \langle \mathscr{F}^{\parallel} \rangle &= \frac{4\langle F^{\parallel} \rangle}{\pi \rho_0 U_0^2 h^2 N_\infty}, \\ \langle \mathscr{F}^{\perp} \rangle &= \frac{4\langle F^{\perp} \rangle}{\pi \rho_0 U_0^2 h^2 N_\infty}, & \langle \mathscr{Q} \rangle &= \frac{4\langle Q \rangle}{\pi \rho_0 U_0^2 h^2 N_\infty}. \end{aligned}\right\} \tag{5.11}$$

Note that in the normalization factor (Pétrélis *et al.* 2006), h is the height of the topography, U_0 is the barotropic tidal amplitude, and N_∞ is the background value of the buoyancy frequency.

After a couple of initial cycles, the flux reaches a quasi-steady state with an approximately constant amplitude, similar to the results found for other flow statistics.

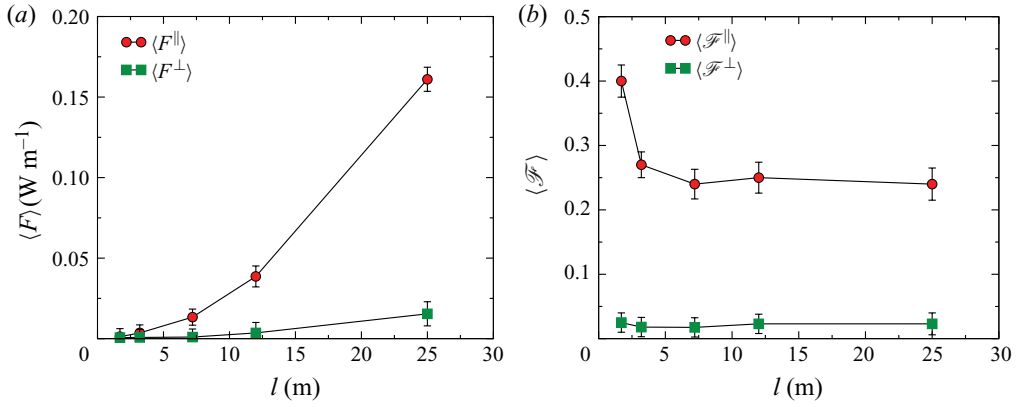

FIGURE 16. (Colour online) (*a*) Cycle-averaged, integrated energy flux in the streamwise direction, $\langle F^{\parallel}\rangle$ (W m^{-1}), and the vertical direction, $\langle F^{\perp}\rangle$ (W m^{-1}), as a function of the slope length. (*b*) Same as for normalized energy fluxes. Here, the normalization factor is $(\pi/4)\rho_0 U_0^2 h^2 N_\infty$, where h is the height of the sloping topography. Time averaging is performed over the final five cycles of the simulation.

The spatial distribution of the streamwise flux, $\langle p_{bc}u_{bc}\rangle_{y,t}$, averaged over five tidal cycles is shown for case 5 in figure 15. Positive values of the flux correspond to rightward-propagating energy and vice versa. In order to evaluate the net streamwise flux carried by the beam, the flux is integrated over the vertical dashed lines in the figure. The net energy flux is outward on these vertical boundaries, rightward on the right boundary and leftward on the left boundary. Above and on the right of the slope, the internal wave flux is strong and concentrated into a beam. On the lower left portion, the beam widens and the internal wave flux weakens owing to dissipation associated with interaction with the flat portion of the bottom. Consequently, the magnitude of the rightward streamwise flux, $\int_{h(x_2)}^{z_2} F^{\parallel}|_{x_2}\,\mathrm{d}z$, is substantially larger relative to the magnitude of the leftward streamwise flux $\int_{h(x_1)}^{z_2} F^{\parallel}|_{x_1}\,\mathrm{d}z$.

A comparative study is performed for the five cases based upon the net horizontal flux, $\langle F^{\parallel}\rangle$ (sum of the outward fluxes on the left and right boundaries) and the net vertical flux $\langle F^{\perp}\rangle$ (the outward flux on top boundary) and the results are plotted in figure 16(*a*). The horizontal energy flux, $\langle F^{\parallel}\rangle$, dominates the vertical component. Both energy fluxes increase with increasing slope length. The linear theory of internal tides leads to the result that the internal wave flux is proportional to $(\pi/4)\rho_0 U_0^2 h^2 N_\infty$ with h being the slope height. Therefore, the energy flux increases with increasing slope length. The net normalized horizontal flux ($\langle \mathscr{F}^{\parallel}\rangle$), which uses the linear scaling for normalization, is plotted as a function of the slope length in figure 16(*b*). The normalized value initially decreases and then seems to saturate at higher values of the slope length. The initial decrease occurs because conversion to turbulence increases, as will be quantified in the next section. The saturation occurs because eventually, for high-enough Reynolds numbers, a constant fraction of the linear estimate of the internal wave flux is lost to local turbulence and locally trapped waves. This explanation assumes that nonlinearity and turbulence do not fundamentally alter the scaling law of internal wave generation as deduced from linear theory.

The vertical energy flux, $\langle \mathscr{F}^{\perp}\rangle$, which is small compared to $\langle \mathscr{F}^{\parallel}\rangle$, shows a similar dependence on the slope length.

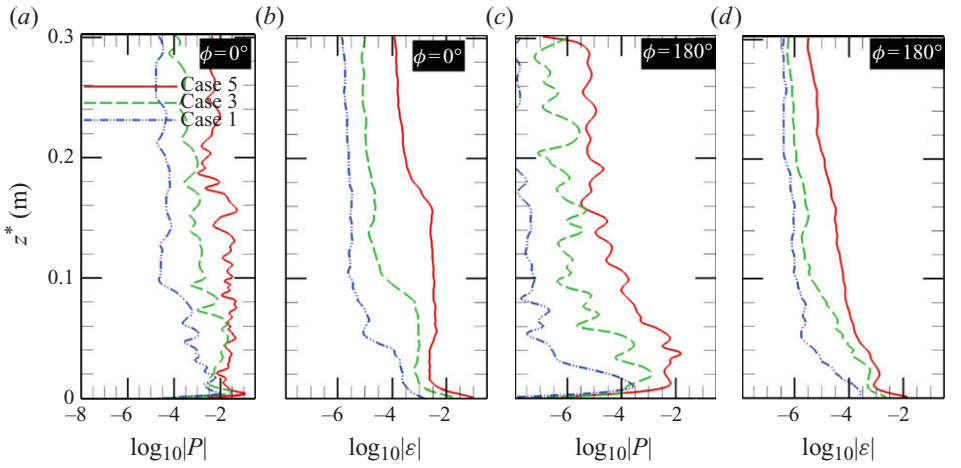

FIGURE 17. (Colour online) Logarithmic profiles of production, $\log_{10}|P|$, and dissipation, $\log_{10}|\varepsilon|$, as a function of height above the bottom at location Q in the inset in figure 4. Plots (a, b) correspond to $\phi = 0°$, when the upslope bottom flow peaks, while (c, d) correspond to $\phi = 180°$, when the downslope bottom flow peaks.

6. Turbulence energetics

Turbulence statistics are computed using spanwise averages. The turbulent kinetic energy, $K = 1/2\langle u_i' u_i' \rangle_y$ also denoted by TKE, represents the energy in fluctuations with respect to the mean velocity and satisfies the following evolution equation:

$$\frac{\partial K}{\partial t} + \langle u \rangle_y \frac{\partial K}{\partial x} + \langle w \rangle_y \frac{\partial K}{\partial z} = P - \varepsilon + B - \frac{\partial T_x}{\partial x} - \frac{\partial T_z}{\partial z}. \tag{6.1}$$

Here, $\partial T_x/\partial x$ and $\partial T_z/\partial z$, which correspond to the transport of the TKE, consist of pressure transport, turbulent transport, viscous transport and SGS transport:

$$\left.\begin{aligned} T_x &\equiv \frac{1}{\rho_0}\langle p' u' \rangle_y + \frac{1}{2}\langle u_i' u_i' u' \rangle_y - \nu \frac{\partial K}{\partial x} + \langle \tau_{i1}' u_i' \rangle_y, \\ T_z &\equiv \frac{1}{\rho_0}\langle p' w' \rangle_y + \frac{1}{2}\langle u_i' u_i' w' \rangle_y - \nu \frac{\partial K}{\partial z} + \langle \tau_{i3}' u_i' \rangle_y. \end{aligned}\right\} \tag{6.2}$$

Also, P is the production term defined as

$$P \equiv -\langle u_i' u_j' \rangle_y \langle S_{ij} \rangle_y - \langle \tau_{ij} \rangle_y \langle S_{ij} \rangle_y, \tag{6.3}$$

where the last term is the SGS production. The turbulent dissipation rate, ε, is defined as the sum of the resolved and SGS components:

$$\varepsilon \equiv \nu \left\langle \frac{\partial u_i'}{\partial x_j} \frac{\partial u_i'}{\partial x_j} \right\rangle_y - \langle \tau_{ij} S_{ij} \rangle_y . \tag{6.4}$$

Finally, B is the buoyancy flux defined as

$$B \equiv -\frac{g}{\rho_0}\langle \rho' w' \rangle_y. \tag{6.5}$$

Profiles of turbulent production and dissipation are plotted at location Q on the slope as a function of height above the bottom in figure 17. Results for cases 1, 3 and 5 corresponding to slope lengths of 1.7, 7.2 and 25.0 m are shown at two

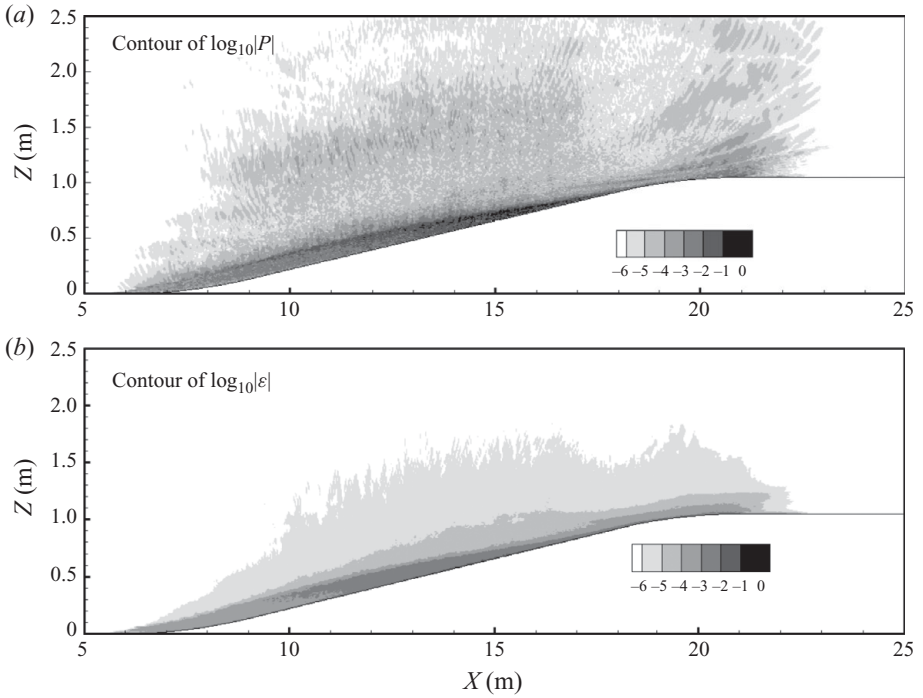

FIGURE 18. Case 4 at a time corresponding to $\phi = 0°$: (a) contours of turbulent production and (b) contours of turbulent dissipation.

phases: $\phi = 0°$, corresponding to the peak value of the upward bottom velocity, and $\phi = 180°$, corresponding to the peak value of the downward velocity. At $\phi = 0°$, the turbulent production shown in figure 17(a) peaks near the bottom boundary while the turbulent dissipation shown in figure 17(b) peaks at the bottom boundary, as is typical for boundary-layer turbulence. Both production and dissipation increase with the slope length. The turbulent production and dissipation at $\phi = 180°$, shown in figure 17(c, d), exhibit profiles that have faster decay rates relative to those at $\phi = 0°$. The peak dissipation at the bottom boundary during the peak downslope flow is about an order of magnitude smaller than the corresponding value at $\phi = 0°$. This occurs despite the fact that mean shear is higher during the downslope motion. In the present problem, shear alone does not play a key role in determining the turbulence intensity. During the downslope flow, stratification increases and acts opposite to the shear effect by suppressing the near-wall turbulence.

The spatial distribution of production and dissipation is shown in figure 18(a, b), respectively, for case 4 at a time that corresponds to $\phi = 0°$. Although the largest values of production are found in the tidal beam and the associated boundary layer at the slope, a significant amount of production is also found outside of the boundary layer where it is associated with other temporal harmonics that propagate out at angles that are larger than the beam angle. Unlike production, the maximum value of dissipation ($\sim 1\,\mathrm{m^2\,s^{-3}}$) is limited to the slope. Nevertheless, there are some patches of dissipation on the flat topography adjacent to the slope.

Profiles of the turbulent kinetic energy, K, at a location midway up the slope are shown in figure 19(a) at a time which corresponds to $\phi \sim 0°$. The TKE reaches maximum value close to the bottom boundary and then decreases with increasing height from the bottom. With increasing length of the slope, the magnitude of K

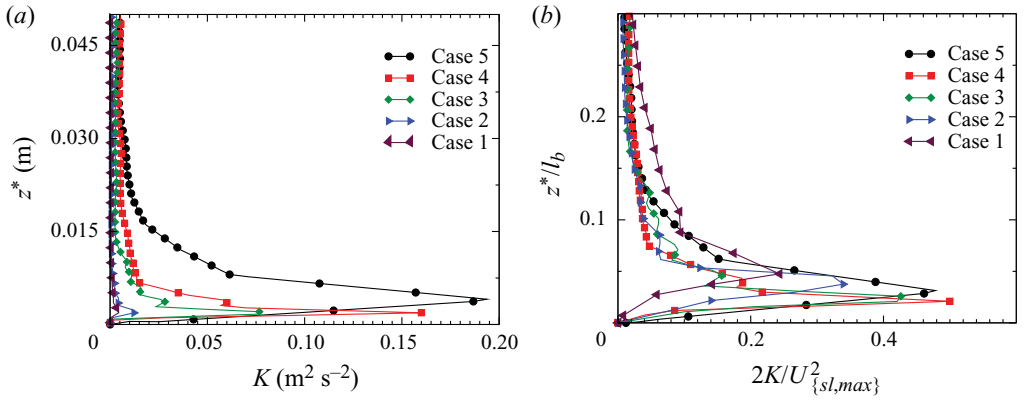

FIGURE 19. (Colour online) (*a*) Turbulent kinetic energy profile as a function of height, z^*, above the bottom at the midpoint of the slope shown in the inset of figure 4. (*b*) Same TKE profiles replotted after normalization.

is enhanced. The location of peak K also shifts upwards with increasing slope length. Figure 19(*b*) shows profiles of K at the same location and time, plotted after normalization with the peak mean velocity $U_{sl,max}$ and the beam thickness, l_b. This normalization significantly decreases variation between cases.

Figure 20(*b*) shows the temporal evolution of each term in the K budget along with the turbulent kinetic energy for case 3 at the midpoint of the slope and at a location close to the bottom. In order to illustrate the phasing of these quantities, the evolution of streamwise velocity at the same location is given in figure 20(*a*). The production increases shortly after the onset of the upslope boundary flow to enhance the turbulent kinetic energy, clearly visible in the curve corresponding to the TKE during this phase, and reaches maximum value soon after the maximal upward boundary flow. Peak production is followed closely by peak dissipation that occurs during the decelerating phase of the upslope flow. Both turbulent production and dissipation have much smaller values during the downslope flow. The buoyancy flux and transport terms are significant and correspond to turbulence-generated internal waves propagating away from the bottom, as discussed extensively by Gayen *et al.* (2010) in the context of an oscillating boundary layer over a non-sloping bottom.

The behaviour of production, dissipation, buoyancy flux and transport terms at a location twice as far from the bottom surface is illustrated as a function of time in figure 20(*c*). At this location, the dissipation is insignificant while production, buoyancy flux and transport dominate. The turbulent production and the buoyancy flux serve to increase the TKE during the decelerating phase of the upslope flow. Higher up in the boundary layer, turbulent kinetic energy, production and dissipation lag in-phase compared to near-boundary values, similar to the case of a non-sloping bottom reported by Gayen *et al.* (2010).

Time-averaged and area-integrated TKE, dissipation, production and buoyancy flux are denoted by $\langle K\rangle$, $\langle D\rangle$, $\langle B\rangle$ and $\langle P\rangle$:

$$\langle K\rangle = \frac{\rho_0}{2nT}\int_{nT}\int_{\Gamma}\left[\langle u'^2\rangle_y + \langle v'^2\rangle_y + \langle w'^2\rangle_y\right]\mathrm{d}A\,\mathrm{d}t, \tag{6.6}$$

$$\langle P\rangle = -\frac{\rho_0}{nT}\int_{nT}\int_{\Gamma}\left[\langle u_i'u_j'\rangle_y\frac{\partial\langle u_i\rangle_y}{\partial x_j} + \langle\tau_{ij}\rangle_y\langle S_{ij}\rangle_y\right]\mathrm{d}A\,\mathrm{d}t, \tag{6.7}$$

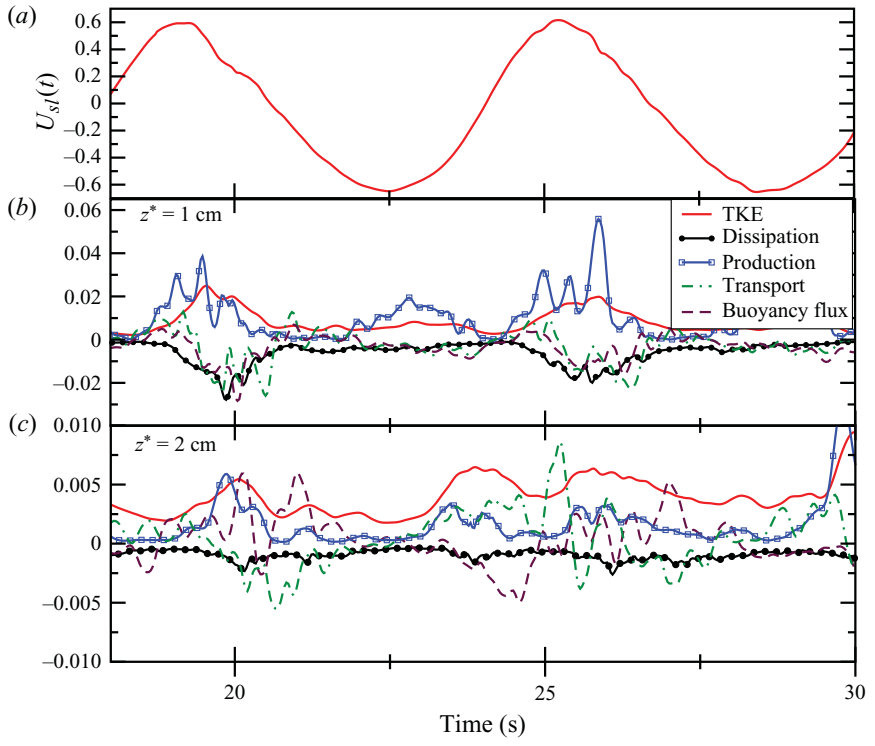

FIGURE 20. (Colour online) Time evolution in case 3. (*a*) Stream velocity is shown as a function of time at a location midpoint of a slope and 1 cm above the bottom. Temporal evolution of turbulent kinetic energy, production, dissipation, buoyancy flux and modified transport is shown in (*b*,*c*) at the midpoint of the slope at locations 1 and 2 cm above the bottom. The unit for TKE is $\mathrm{m^2\,s^{-2}}$, whereas the unit of other terms in the energy budget is $\mathrm{m^2\,s^{-3}}$.

$$\langle D\rangle = \frac{\rho_0}{nT}\int_{nT}\int_{\Gamma}\left[\nu\left\langle\frac{\partial u_i'}{\partial x_j}\frac{\partial u_i'}{\partial x_j}\right\rangle_y - \langle\tau_{ij}S_{ij}\rangle_y\right]\mathrm{d}A\,\mathrm{d}t, \tag{6.8}$$

$$\langle B\rangle = -\frac{\rho_0}{nT}\int_{nT}\int_{\Gamma}\left[\frac{g}{\rho_0}\langle\rho' w'\rangle_y\right]\mathrm{d}A\,\mathrm{d}t. \tag{6.9}$$

Normalized values are defined as follows:

$$\langle\mathscr{K}\rangle = \frac{2\langle K\rangle}{\rho_0 U_0^2\Gamma}, \quad \langle\mathscr{P}\rangle = \frac{4\langle P\rangle}{\pi\rho_0 U_0^2 h^2 N_\infty}, \quad \langle\mathscr{D}\rangle = \frac{4\langle D\rangle}{\pi\rho_0 U_0^2 h^2 N_\infty}, \quad \langle\mathscr{B}\rangle = \frac{4\langle B\rangle}{\pi\rho_0 U_0^2 h^2 N_\infty}. \tag{6.10}$$

The normalization of the turbulent kinetic energy, $\langle K\rangle$, is the same as that of the kinetic energy density, $\langle E_k\rangle$, discussed previously, while that of $\langle P\rangle$ and $\langle D\rangle$ is the same as was used for the internal wave flux, $\langle\mathscr{F}\rangle$. Figure 21 shows that $\langle\mathscr{K}\rangle$, production $\langle\mathscr{P}\rangle$, dissipation $\langle\mathscr{D}\rangle$ and buoyancy production $\langle\mathscr{B}\rangle$ increase with increasing slope length. The curves also become flatter with increasing slope length. The integrated turbulent production is larger than the integrated dissipation. The integrated buoyancy flux is also significant. The data shown in figure 21(*b*) can be compared to the streamwise internal wave flux, $\langle\mathscr{F}^{\parallel}\rangle$, as discussed earlier in figure 16. For instance, in case 5 with slope length of 25 m, the integrated turbulent production is approximately 18 % and

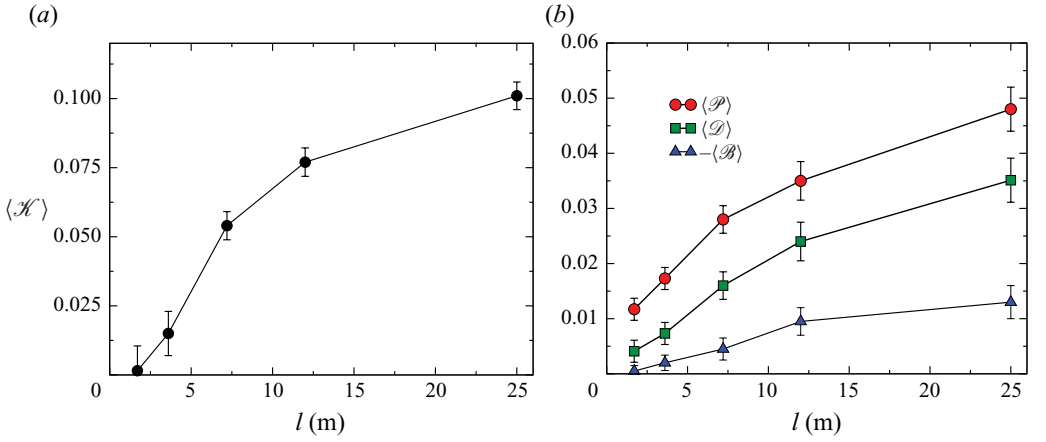

FIGURE 21. (Colour online) (*a*) Normalized value of the integrated TKE, $\langle \mathscr{K} \rangle$, as a function of the slope length. (*b*) Normalized values of production $\langle \mathscr{P} \rangle$, dissipation $\langle \mathscr{D} \rangle$ and buoyancy flux $\langle \mathscr{B} \rangle$. Here, $\langle \mathscr{K} \rangle$ is normalized by $(1/2)\rho_0 U_0^2 \Gamma$, whereas the normalization for $\langle \mathscr{P} \rangle$, $\langle \mathscr{D} \rangle$ and $\langle \mathscr{B} \rangle$ is $(\pi/4)\rho_0 U_0^2 h^2 N_\infty$.

the integrated turbulent dissipation is approximately 12 % of the streamwise wave flux.

7. Conclusions

DNS and LES approaches have been used to investigate the dynamics of a stratified flow over a sloping bottom under an oscillating tidal flow. The three-dimensional, unsteady simulations are performed in coordinates that conform to the bottom topography. A dynamic eddy-viscosity model is used for LES and the near-bottom turbulence is resolved at the moderate Reynolds numbers considered here. The background stratification is such that the critical slope angle is 5°, a small value as is typical in the ocean. The slope length, l, is varied between 1.7 and 25 m to quantify its influence. The excursion number is chosen to be small in all cases as is typical for bottom topography in deep water.

Resonant generation of internal waves at the near-critical slope simulated here leads to an internal wave beam (where the kinetic energy and wave energy flux are concentrated) that leaves the slope and to a boundary layer under the intensified wave velocity. There is transition to turbulence in the boundary flow leading to enhanced viscous dissipation that regularizes the resonant response so that an oscillating boundary layer in quasi-steady state forms at the slope. The velocity profile, with a strong near-bottom jet (corresponding to the internal wave beam) and spatial oscillations as a function of the vertical coordinate, is qualitatively different from the oscillating boundary layer on a non-sloping bottom. The peak velocity is found to increase at approximately $l^{0.45}$ in the turbulent regime, which is different from that in the laminar regime due to length dependence of the effective turbulent viscosity. An analytical expression that incorporates the observed length dependence of turbulent viscosity leads to a scaling law for the peak bottom velocity which is in good agreement with the scaling observed in the simulations. The width of the beam also increases according to a power law as a function of the slope length. It is worth noting that the peak velocity and the width of the beam cannot increase indefinitely

because the region with uninterrupted critical slope is finite in realistic topography. The baroclinic velocity shows significant temporal and spatial variability. The internal wave response leads to an upslope-moving tidal front which propagates shorewards as a turbulent gravity current.

The velocity spectrum on the slope and inside the boundary layer shows discrete peaks at the fundamental, harmonics, subharmonic and interharmonics that correspond to topography-generated waves superposed on a continuous spectrum associated with broadband turbulence. The energy content in higher harmonics relative to that in the fundamental increases with the slope length so that the second harmonic contains about 15% of the energy in the fundamental when the slope length is $l = 25$ m, the largest value in the present simulations. The velocity spectrum at points outside the boundary layer and with little turbulence show more prominent discrete peaks as well as a continuous spectrum. Turbulence-generated waves and wave–wave interactions among topographic waves are responsible for the continuous spectrum at these points.

Turbulent kinetic energy and dissipation rates increase substantially and the locations of their peaks move upwards with increasing slope length, l. Normalization of the profiles with the beam width and the maximum slope velocity substantially reduces the variation between cases. The integrated normalized value of turbulent production is larger than the corresponding value of turbulent dissipation. In the case of the longest slope of $l = 25$ m, the integrated production and turbulent dissipation are found to be 18 % and 12 %, respectively, of the energy flux associated with the internal tide. The profiles of turbulent production and dissipation depend on the phase of the internal tide and are significantly fuller than profiles observed in the boundary layer below an oscillating current without internal wave generation.

The dimensional baroclinic energy flux increases with the slope length. The non-dimensional baroclinic energy flux, $\langle \mathscr{F}^{\parallel} \rangle$, has also been computed with a normalization factor, $(\pi/4)\rho_0 U_0^2 h^2 N_\infty$, taken from linear theory. The value of $\langle \mathscr{F}^{\parallel} \rangle$ shows a maximum value of 0.4 (or 40 %) for the smallest slope, $l = 1.7$ m, decreases with increasing l, and appears to approach a saturation value, $\langle \mathscr{F}^{\parallel} \rangle \simeq 0.25$. The substantial increase of conversion to turbulence with increasing slope length (turbulent production as high as 18 % of the internal wave flux when $l = 25$ m) is a likely contributor to the decrease in the normalized flux, $\langle \mathscr{F}^{\parallel} \rangle$, with increasing slope length and its potential saturation.

We acknowledge financial support through NSF grant 0825705 (programme manager Eric Itsweire).

Appendix. Decomposition of pressure and velocity

Decomposition into barotropic and barotropic (internal tide) components can be performed in different ways (Holloway 1996; Kunze *et al.* 2002; Khatiwala 2003; Nash *et al.* 2004, 2006; Gerkema & van Haren 2007). Here, we follow Nash *et al.* (2004, 2006). The baroclinic wave velocity is defined by

$$\boldsymbol{u}_{bc}(\boldsymbol{x}, t) = \boldsymbol{u}(\boldsymbol{x}, t) - \widehat{\boldsymbol{u}}(\boldsymbol{x}) - \boldsymbol{u}_b(t, x, y), \tag{A 1}$$

where the residual velocity $\widehat{\boldsymbol{u}}(\boldsymbol{x}) = (1/5T) \int_t^{5T+t} \boldsymbol{u}(\boldsymbol{x}, t)\, \mathrm{d}t$ is a cycle-averaged mean and $\boldsymbol{u}_b(t, y, z)$ is calculated by enforcing baroclinicity:

$$\int_{h(x)}^{l_z} \boldsymbol{u}_{bc}(\boldsymbol{x}, t)\, \mathrm{d}z = 0. \tag{A 2}$$

Here, $h(x)$ is the height of the slope topography with respect to the left flat bottom. Note that, for the present problem with a small slope angle, $\boldsymbol{u}_b(t, y, z)$ is approximately equal to the oscillatory current resulting from the imposed oscillatory pressure gradient and its dependence on y and z is weak while the residual velocity $\widehat{u}(\boldsymbol{x})$ is very small.

The density anomaly is estimated at $\rho_{bc}(\boldsymbol{x}, t) = \rho(\boldsymbol{x}, t) - \widehat{\rho}(\boldsymbol{x}) - \rho_b(t, x, y)$, where $\widehat{\rho}(\boldsymbol{x})$ is the average over five tidal cycles. Here $\rho_b(t, x, y)$ is calculated by enforcing baroclinicity similar to the baroclinic wave velocity in (A 2). The pressure anomaly is calculated imposing hydrostatic balance,

$$p_{bc}(\boldsymbol{x}, t) = p_s(t, y, z) + \int_z^{l_z} \rho_{bc}(\boldsymbol{x}, t) g \, \mathrm{d}z'. \tag{A 3}$$

The surface contribution, $p_s(t, y, z)$, of the baroclinic motion is computed using the constraint of zero depth-average of the baroclinic pressure perturbation, i.e.

$$\int_{h(x)}^{l_z} p_{bc}(\boldsymbol{x}, t) \, \mathrm{d}z = 0. \tag{A 4}$$

REFERENCES

Akhavan, R., Kamm, R. D. & Shapiro, A. H. 1991 An investigation of transition to turbulence in bounded oscillatory Stokes flows. Part 2. Numerical simulations. *J. Fluid Mech.* **225**, 423–444.

Armenio, V. & Sarkar, S. 2002 An investigation of stably stratified turbulent channel flow using large-eddy simulation. *J. Fluid Mech.* **459**, 1–42.

Baines, P. G. 1974 The generation of internal tides over steep continental slopes. *Phil. Trans. R. Soc. Lond.* A **277**, 27–58.

Baines, P. G. 1982 On internal tide generation models. *Deep-Sea Res.* **29**, 307–338.

Balmforth, N. J., Ierley, G. R. & Young, W. R. 2002 Tidal conversion by subcritical topography. *J. Phys. Oceanogr.* **32**, 2900–2914.

Balmforth, N. J. & Peacock, T. 2009 Tidal conversion by supercritical topography. *J. Phys. Oceanogr.* **39**, 1965–1974.

Bell, T. H. 1975*a* Lee waves in stratified fluid with simple harmonic time dependence. *J. Fluid Mech.* **67**, 705–722.

Bell, T. H. 1975*b* Topographically generated internal waves in the open ocean. *J. Geophys. Res.* **80**, 320–327.

Cacchione, D. A., Pratson, L. F. & Ogston, A. S. 2002 The shaping of continental slopes by internal tides. *Science* **296**, 724–727.

Carter, G. S. & Gregg, M. C. 2002 Intense, variable mixing near the head of Monterey Submarine Canyon. *J. Phys. Oceanogr.* **32**, 3145–3165.

Costamagna, P., Vittori, G. & Blondeaux, P. 2003 Coherent structures in oscillatory boundary layers. *J. Fluid. Mech.* **474**, 1–33.

Dauxois, T. & Young, W. R. 1999 Near-critical reflection of internal waves. *J. Fluid Mech.* **390**, 271–295.

Echeverri, P., Flynn, M. R., Winters, K. B. & Peacock, T. 2009 Low-mode internal tide generation by topography: an experimental and numerical investigation. *J. Fluid Mech.* **636**, 91–108.

Fletcher, C. A. J. 1991 *Computational Techniques for Fluid Dynamics*, 2nd edn. Springer.

Garrett, C. & Kunze, E. 2007 Internal tide generation in the deep ocean. *Annu. Rev. Fluid Mech.* **39**, 57–87.

Gayen, B. & Sarkar, S. 2010 Turbulence during the generation of internal tide on a critical slope. *Phys. Rev. Lett.* **104**, 218502.

Gayen, B., Sarkar, S. & Taylor, J. R. 2010 Large eddy simulation of a stratified boundary layer under an oscillatory current. *J. Fluid Mech.* **643**, 233–266.

Gerkema, T. & van Haren, H. 2007 Internal tides and energy fluxes over Great Meteor Seamount. *Ocean Sci.* **3**, 441–449.

Germano, M., Piomelli, U., Moin, P. & Cabot, W. H. 1991 A dynamic subgrid-scale eddy viscosity model. *Phys. Fluids* **3** (7), 1760–1765.

Gostiaux, L. & Dauxois, T. 2007 Laboratory experiments on the generation of internal tidal beams over steep slopes. *Phys. Fluids* **19**, 028102.

Griffiths, S. D. & Grimshaw, R. H. J. 2007 Internal tide generation at the continental shelf modeled using a modal decomposition: two-dimensional results. *J. Phys. Oceanogr.* **37**, 428–451.

Holloway, P. E. 1996 A numerical model of internal tides with application to the Australian North West Shelf. *J. Phys. Oceanogr.* **26**, 21–37.

Holloway, P. E. & Merrifield, M. A. 1999 Internal tide generation by seamounts, ridges, and islands. *J. Geophys. Res.* **104**, 25937–25951.

Ivey, G. N. & Nokes, R. I. 1989 Vertical mixing due to the breaking of critical internal waves on sloping boundaries. *J. Fluid Mech.* **204**, 479–500.

Jensen, B. L., Sumer, B. M. & Fredsøe, J. 1989 Turbulent oscillatory boundary layers at high Reynolds numbers. *J. Fluid Mech.* **206**, 265–297.

Khatiwala, S. 2003 Generation of internal tides in an ocean of finite depth: analytical and numerical calculations. *Deep-Sea Res.* I **50**, 3–21.

Klymak, J. M., Moum, J. N., Nash, J. D., Kunze, E., Girton, J. B., Carter, G. S., Lee, C. M., Sanford, T. B. & Gregg, M. C. 2006 An estimate of tidal energy lost to turbulence at the Hawaiian Ridge. *J. Phys. Oceanogr.* **36**, 1148–1164.

Korobov, A. S. & Lamb, K. G. 2008 Interharmonics in internal gravity waves generated by tide–topography interaction. *J. Fluid Mech.* **611**, 61–95.

Kunze, E., Rosenfeld, L. K., Carter, G. S. & Gregg, M. C. 2002 Internal waves in Monterey Submarine Canyon. *J. Phys. Oceanogr.* **32**, 1890–1913.

Kunze, E. & Toole, J. M. 1997 Tidally driven vorticity, diurnal shear and turbulence atop Fieberling Seamount. *J. Phys. Oceanogr.* **27**, 2663–2693.

Ledwell, J. R., Montgomery, E. T., Polzin, K. L., St Laurent, L. C., Schmitt, R. W. & Toole, J. M. 2000 Evidence of enhanced mixing over rough topography in the abyssal ocean. *Nature* **403**, 179–182.

Legg, S. 2004 Internal tides generated on a corrugated continental slope. Part II. Along-slope barotropic forcing. *J. Phys. Oceanogr.* **34**, 1824–1838.

Legg, S. & Klymak, J. M. 2008 Internal hydraulic jumps and overturning generated by tidal flows over a tall steep ridge. *J. Phys. Oceanogr.* **38**, 1949–1964.

Li, M., Radhakrishnan, S., Piomelli, U. & Geyer, W. R. 2010 Large-eddy simulation of the tidal-cycle variations of an estuarine boundary layer. *J. Geophys. Res.* **115**, C08003, pp. 1–18.

Lim, K., Ivey, G. N. & Jones, N. L. 2010 Experiments on the generation of internal waves over continental shelf topography. *J. Fluid Mech.* **663**, 385–400.

Llewellyn Smith, S. G. & Young, W. R. 2002 Conversion of the barotropic tide. *J. Phys. Oceanogr.* **32**, 1554–1566.

Llewellyn Smith, S. G. & Young, W. R. 2003 Tidal conversion at a very steep ridge. *J. Fluid Mech.* **495**, 175–191.

Lueck, R. G. & Mudge, T. D. 1997 Topographically induced mixing around a shallow seamount. *Science* **276**, 1831–1833.

Lund, T. S. 1997 On the use of discrete filters for large eddy simulation. In *Annual Research Briefs*, pp. 83–95. Center for Turbulence research, NASA Ames-Stanford University.

Merrifield, M. A., Holloway, P. E. & Johnston, T. M. S. 2001 The generation of internal tides at the Hawaiian Ridge. *Geophys. Res. Lett.* **28**, 559–562.

Moum, J. N., Caldwell, D. R., Nash, J. D. & Gunderson, G. D. 2002 Observations of boundary mixing over the continental slope. *J. Phys. Oceanogr.* **32**, 2113–2130.

Munk, W. & Wunsch, C. 1998 Abyssal recipes II: energetics of tidal and wind mixing. *Deep-Sea Res.* I **45**, 1977–2010.

Nash, J. D., Alford, M. H., Kunze, E., Martini, K. & Kelly, S. 2007 Hotspots of deep ocean mixing on the Oregon continental slope. *Geophys. Res. Lett.* **34**, L01605.

Nash, J. D., Kunze, E., Lee, C. M. & Sanford, T. B. 2006 Structure of the baroclinic tide generated at Kaena Ridge, Hawaii. *J. Phys. Oceanogr.* **36**, 1123–1135.

Nash, J. D., Kunze, E., Toole, J. M. & Schmitt, R. W. 2004 Internal tide reflection and turbulent mixing on the continental slope. *J. Phys. Oceanogr.* **34**, 1117–1134.

Pétrélis, F., Llewellyn Smith, S. G. & Young, W. R. 2006 Tidal conversion at submarine ridge. *J. Phys. Oceanogr.* **36**, 1053–1071.

Polzin, K. L., Oakey, N. S., Toole, J. M. & Schmitt, R. W. 1996 Fine structure and microstructure characteristics across the north west Atlantic subtropical front. *J. Geophys. Res.* **101**, 14111–14121.

Polzin, K. L., Toole, J. M., Ledwell, J. R. & Schmitt, R. W. 1997 Spatial variability of turbulent mixing in the abyssal ocean. *Science* **276**, 93–96.

Radhakrishnan, S. & Piomelli, U. 2008 Large-eddy simulation of oscillating boundary layers: model comparison and validation. *J. Geophys. Res.* **113**, C02022.

Robinson, R. M. 1969 The effects of a barrier on internal waves. *Deep-Sea Res.* **16**, 421–429.

Rudnick, D. L., Boyd, T. J., Brainard, R. E., Carter, G. S., Egbert, G. D., Gregg, M. C., Holloway, P. E., Klymak, J. M., Kunze, E., Lee, C. M., Levine, M. D., Luther, D. S., Martin, J. P., Merrifield, M. A., Moum, J. N., Nash, J. D., Pinkel, R., Rainville, L. & Sanford, T. B. 2003 From tides to mixing along the Hawaiian Ridge. *Science* **301**, 355–357.

Sakamoto, K. & Akitomo, K. 2008 The tidally induced bottom boundary layer in a rotating frame: similarity of turbulence. *J. Fluid Mech.* **615**, 1–25.

Salon, S., Armenio, V. & Crise, A 2007 A numerical investigation of the Stokes boundary layer in the turbulent regime. *J. Fluid Mech.* **570**, 253–296.

Slinn, D. N. & Riley, J. J. 1998 Turbulent dynamics of a critically reflecting internal gravity wave. *Theoret. Comput. Fluid Dyn.* **11**, 281–303.

Spalart, P. R. & Bladwin, B. S. 1987 Direct simulation of a turbulent oscillating boundary layer. In *Turbulent Shear Flows*, vol. 6, pp. 417–440. Springer.

St Laurent, L. C. & Garrett, C. 2002 The role of internal tides in mixing the deep ocean. *J. Phys. Oceanogr.* **32**, 2882–2899.

St Laurent, L. C., Stringer, S., Garrett, C. & Perrault-Joncas, D. 2003 The generation of internal tides at abrupt topography. *Deep-Sea Res.* I **50**, 987–1003.

St Laurent, L. C., Toole, J. M. & Schmitt, R. W. 2001 Buoyancy forcing by turbulence above rough topography in the abyssal Brazil Basin. *J. Phys. Oceanogr.* **31**, 3476–3495.

Taylor, J. R. & Sarkar, S. 2007 Internal gravity waves generated by a turbulent bottom Ekman layer. *J. Fluid Mech.* **590** (1), 331–354.

Taylor, J. R. & Sarkar, S. 2008*a* Direct and large eddy simulations of a bottom Ekman layer under an external stratification. *Intl J. Heat Fluid Flow* **29**, 721–732.

Taylor, J. R. & Sarkar, S. 2008*b* Stratification effects in a bottom Ekman layer. *J. Phys. Oceanogr.* **38** (11), 2535–2555.

Thorpe, S. A. 1992 Thermal fronts caused by internal gravity waves reflecting from a slope. *J. Phys. Oceanogr.* **22**, 105–108.

Venayagamoorthy, S. K. & Fringer, O. B. 2007 On the formation and propagation of nonlinear internal boluses across a shelf break. *J. Fluid. Mech.* **577**, 137–159.

Vittori, G. & Verzicco, R. 1998 Direct simulation of transition in an oscillatory boundary layer. *J. Fluid Mech.* **371**, 207–232.

Vreman, B., Geurts, B. & Kuerten, H. 1997 Large-eddy simulation of the turbulent mixing layer. *J. Fluid Mech.* **339**, 357–390.

Wunsch, C. & Ferrari, R. 2004 Vertical mixing, energy, and the general circulation of the oceans. *Annu. Rev. Fluid Mech.* **36**, 281–314.

Zang, Y., Street, R. L. & Koseff, J. R. 1993 A dynamic mixed subgrid-scale model and its application to turbulent recirculating flows. *Phys. Fluids* A **5** (12), 3186–3196.

Zeeuw, P. M. De 1990 Matrix-dependent prolongations and restrictions in a blackbox multigrid solver. *J. Comp. Appl. Math.* **33**, 1–27.

Zhang, H. P., King, B. & Swinney, H. L 2008 Resonant generation of internal waves on a model continental slope. *Phys. Rev. Lett.* **100**, 244504.